Computers and Mathematics with Applications 77 (2019) 1703–1721

Contents lists available at ScienceDirect

Computers and Mathematics with Applications

journal homepage: www.elsevier.com/locate/camwa

A high-order absorbing boundary condition for 2D time-harmonic elastodynamic scattering problems

V. Mattesi [a,*], M. Darbas [b], C. Geuzaine [a]

[a] Department of Electrical Engineering and Computer Science, University of Liège, Belgium
[b] LAMFA, University of Picardie Jules Verne, Amiens, France

ARTICLE INFO

Article history:
Received 30 January 2018
Received in revised form 7 May 2018
Accepted 14 May 2018
Available online 6 June 2018

Keywords:
Scattering
2D time-harmonic elastic waves
Absorbing boundary condition
High-frequency

ABSTRACT

In this paper, we are concerned with the construction of a new high-order Absorbing Boundary Condition (ABC) for 2D-elastic scattering problems. It is defined by an approximate local Dirichlet-to-Neumann (DtN) map. First, we explain the derivation of this approximation. Next, a detailed analytical study in terms of Hankel functions in the circular case is addressed. The new ABC is compared with the standard low-order Lysmer–Kuhlemeyer ABC. Finally, its accuracy and efficiency are investigated for various numerical examples, particularly at high frequencies.

1. Introduction

The paper is concerned with the numerical solution of high-frequency scattering problems of time-harmonic elastic waves by a two-dimensional rigid obstacle. The accurate numerical modeling of high-oscillatory elastic problems is a timely research field with a large panel of possible applications. From seismology and non-destructive testing to medical ultrasound, various numerical methods can be used to solve scattering problems in unbounded domains [1]. For methods like finite elements, the unbounded domain must be truncated using a fictitious boundary at finite distance, on which a non-reflecting boundary condition is imposed. This is the point of view we adopt here. In the ideal configuration, the boundary condition is "transparent" in the sense that the solution in the truncated domain is exactly the restriction of the outgoing solution in the unbounded domain. However, such a boundary condition is generally non-local and too expensive numerically. Local boundary conditions are thus of interest. Such non-reflecting boundary conditions are also called Absorbing Boundary Conditions and consist in constructing local approximations of the Dirichlet-to-Neumann map. The main objective is to obtain ABCs that minimize the spurious reflections generated by the fictitious boundary. For acoustic wave problems, well-known examples are the Clayton–Engquist [2], Engquist–Majda [3] and the Bayliss–Turkel conditions [4]. For elasticity, without being exhaustive, we can cite [5–7] for exact non-local boundary conditions and [8–10] for local approximate boundary conditions. Compared to alternative approaches such as Perfect Matched Layer methods [11,12], which deal with infinite media by adding a small layer of finite elements around the truncated domain of study, local ABCs can be easily used as transmission conditions in the context of domain decomposition methods [13].

The aim of this paper is to derive a high-order ABC for 2D time-harmonic elastodynamic scattering problems by adapting ideas from Chaillat, Darbas and Le Louër [10] for the construction of accurate approximations of the elastodynamic Dirichlet-to-Neumann map in the context of analytical preconditioning techniques for boundary integral equations and in the context of On-Surface Radiation Conditions (OSRC). The paper is organized as follows. We introduce in Section 2 the problem under study and the low-order Lysmer–Kuhlemeyer ABC [8]. In Section 3, we derive an exact DtN operator in the case of the

* Corresponding author.
E-mail address: vanessa.mattesi@ulige.be (V. Mattesi).

https://doi.org/10.1016/j.camwa.2018.05.014
0898-1221/

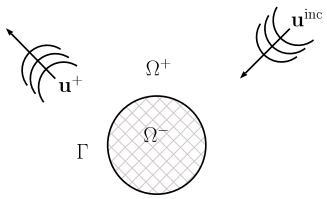

Fig. 1. Scattering wave problem.

half-plane using Fourier analysis. Then, we obtain a local approximate DtN map for a general smooth surface thanks to a regularization process and a Padé-local representation of square-root operators. Section 4 is devoted to a detailed analytical study. We describe the general expression of the analytical solutions and determine the damping and Padé parameters. The new ABC is compared with the Lysmer–Kuhlemeyer ABC for different configurations. In Section 5, we express the weak formulation of the considered truncated boundary-value problem in view of the finite element implementation. Section 6 presents numerical results obtained with the open source softwares GetDP and Gmsh [14,15]. Finally, Section 7 gives some concluding remarks and directions for future works.

2. Problem statement

2.1. Exterior Navier problem

Let us consider a bounded domain Ω^- in $\mathbb{R}^2$ representing an impenetrable body with a closed boundary $\Gamma := \partial\Omega$ of class $\mathcal{C}^2$ at least. Let Ω^+ denote the associated exterior domain $\mathbb{R}^2\backslash\overline{\Omega^-}$. The Lamé parameters, μ and λ, and the density ρ are positive constants. We are interested in finding the scattering field $\boldsymbol{u}^+$ generated by an incident wave $\boldsymbol{u}^{\text{inc}}$ striking the obstacle Ω^- (see Fig. 1). The propagation of time-harmonic waves in an isotropic and homogeneous elastic medium is modeled by the Navier equation

$$\operatorname{div}\sigma(\boldsymbol{u}^+) + \rho\omega^2\boldsymbol{u}^+ = 0, \tag{1}$$

where $\omega > 0$ is the angular frequency. In the case of 2D isotropic elastodynamics, the stress and strain tensors are given by $\sigma(\boldsymbol{u}^+) = \lambda(\operatorname{div}\boldsymbol{u}^+)\mathrm{I}_2 + 2\mu\varepsilon(\boldsymbol{u}^+)$ and $\varepsilon(\boldsymbol{u}^+) = \frac{1}{2}\left([\nabla\boldsymbol{u}^+] + [\nabla\boldsymbol{u}^+]^t\right)$ respectively, where I_2 is the 2-by-2 identity matrix and $[\nabla\boldsymbol{u}^+]$ is the matrix whose the jth column is the gradient of the jth component of $\boldsymbol{u}^+$. In solid media (or very viscous), elastic waves can be decomposed into a longitudinal pressure wave and a transversal shear wave. In seismology, the pressure wave is commonly called primary wave (P-wave) and the shear wave is the secondary wave (S-wave). Indeed, the celerity of P-waves is always faster than S-wave speed therefore P-waves are detected first by seismograph stations. Those waves are body waves (volume waves), they propagate through the interior of the earth unlike surface waves (for instance Rayleigh, Love or Stoneley waves) traveling along the earth's surface. We use the notation P-wave and S-wave for pressure wave and shear wave even if the work is not dedicated only to seismology. The displacement field $\boldsymbol{u}^+$ is decomposed into the longitudinal field $\boldsymbol{u}_p = \nabla\psi_p$ and the transverse field $\boldsymbol{u}_s = \boldsymbol{u}^+ - \boldsymbol{u}_p = \mathbf{curl}\,\psi_s$. Notice that in two dimensions, the vector rotational operator is defined for a scalar function φ by $\mathbf{curl}\,\varphi = (\partial_y\varphi, -\partial_x\varphi)^t$, whereas the scalar rotational operator acting on a vector field $\mathbf{v} = (v_x, v_y)^t$ is given by $\operatorname{curl}\mathbf{v} = \partial_x v_y - \partial_y v_x$. The Lamé potentials ψ_p and ψ_s satisfy

$$\begin{cases} \psi_p = -\kappa_p^{-2}\operatorname{div}\boldsymbol{u}^+ \\ \Delta\psi_p + \kappa_p^2\psi_p = 0 \end{cases} \quad \text{and} \quad \begin{cases} \psi_s = \kappa_s^{-2}\operatorname{curl}\boldsymbol{u}^+ \\ \Delta\psi_s + \kappa_s^2\psi_s = 0 \end{cases}, \tag{2}$$

where $\kappa_p^2 = \rho\omega^2/(\lambda + 2\mu)$ and $\kappa_s^2 = \rho\omega^2/\mu$ are the P- and S-wavenumbers. The wavelengths are defined by $\lambda_{\{p,s\}} = 2\pi/\kappa_{\{p,s\}}$. The scattering problem is formulated as follows: given an incident wave field $\boldsymbol{u}^{\text{inc}}$ which is assumed to solve the Navier equation in the absence of any scatterer, find the displacement $\boldsymbol{u}^+$ solution to the Navier equation (1) in Ω^+ which satisfies the Dirichlet boundary condition on Γ

$$\boldsymbol{u}^+_{|\Gamma} = -\boldsymbol{u}^{\text{inc}}_{|\Gamma}. \tag{3}$$

In addition, the field $\boldsymbol{u}^+$ has to satisfy the Kupradze radiation conditions [16] at infinity

$$\lim_{r\to\infty}\sqrt{r}\left(\frac{\partial\psi_p}{\partial r} - i\kappa_p\psi_p\right) = 0, \qquad \lim_{r\to\infty}\sqrt{r}\left(\frac{\partial\psi_s}{\partial r} - i\kappa_s\psi_s\right) = 0, \quad r = |\boldsymbol{x}|, \tag{4}$$

uniformly in all directions.

2.2. Absorbing boundary conditions

To numerically compute the solution to problem (1)–(3)–(4) by using the finite element method, the infinite propagation domain Ω^+ is truncated with a fictitious boundary Γ^∞ enclosing the obstacle (see Fig. 2). Let us denote by Ω the bounded

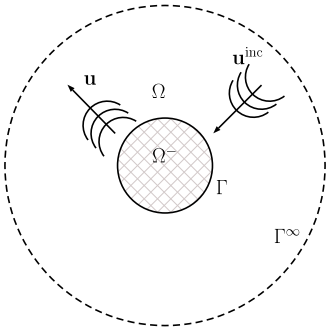

Fig. 2. Truncated problem.

domain delimited by Γ and Γ^∞, and by $\boldsymbol{n} = (n_x, n_y)^t$ the outer unit normal vector to the boundary Γ^∞. An Absorbing Boundary Condition (ABC) is introduced on Γ^∞ to simulate the radiation condition. The resulting bounded boundary-value problem is the following: find $\boldsymbol{u}$ solution to

$$\begin{cases} \operatorname{div}\sigma(\boldsymbol{u}) + \rho\omega^2\boldsymbol{u} = 0, & \text{in } \Omega, \\ \boldsymbol{u}_{|\Gamma} = -\boldsymbol{u}^{\text{inc}}_{|\Gamma}, & \text{on } \Gamma, \\ \boldsymbol{t}_{|\Gamma^\infty} = \mathcal{B}\boldsymbol{u}_{|\Gamma^\infty}, & \text{on } \Gamma^\infty. \end{cases} \tag{5}$$

The Neumann trace, defined by $\boldsymbol{t}_{|\Gamma^\infty} := \boldsymbol{T}\boldsymbol{u}$, is given by the traction operator

$$\boldsymbol{T} = 2\mu\frac{\partial}{\partial \boldsymbol{n}} + \lambda \boldsymbol{n}\operatorname{div} + \mu\, \boldsymbol{n}\times\operatorname{curl}. \tag{6}$$

For a scalar function φ, we have $\boldsymbol{n}\times\varphi = (\varphi n_y, -\varphi n_x)^t$.

Remark 1. In the usual cylindrical coordinates system (r, θ), the traction operator is described by

$$\boldsymbol{T}\boldsymbol{u} := \begin{pmatrix} (\lambda+2\mu)\partial_r p + \lambda\dfrac{\partial_\theta}{r}q + \dfrac{\lambda}{r}p \\ \mu\partial_r q + \mu\dfrac{\partial_\theta}{r}p - \dfrac{\mu}{r}q \end{pmatrix}, \tag{7}$$

with (p, q) the cylindrical components of $\boldsymbol{u}$.

The operator $\mathcal{B}$ is an approximation of the exact exterior Dirichlet-to-Neumann (DtN) map on Γ^∞ which is defined by

$$\begin{array}{rccc} \boldsymbol{\Lambda}^{\text{ex}} : & (H^{\frac{1}{2}}(\Gamma^\infty))^2 & \to & (H^{-\frac{1}{2}}(\Gamma^\infty))^2 \\ & \boldsymbol{u}^+_{|\Gamma^\infty} & \mapsto & \boldsymbol{t}^+_{|\Gamma^\infty} \end{array}. \tag{8}$$

The field $\boldsymbol{u}$ is thus an approximation of the restriction of the scattered field $\boldsymbol{u}^+$ to Ω. The accuracy is linked to the choice of the operator $\mathcal{B}$. In this paper, we derive a high-order ABC for the 2D Navier equation and we compare it with the simplest local ABC: the Kupradze radiation condition at finite distance. This zeroth-order ABC, called also Lysmer–Kuhlemeyer boundary condition [5,8], is defined by

$$\mathcal{B} := \mathcal{B}_0 = i(\lambda+2\mu)\kappa_p \mathrm{I}_{\boldsymbol{n}} + i\mu\kappa_s \mathrm{I}_{\boldsymbol{\tau}}, \tag{9}$$

where $\mathrm{I}_{\boldsymbol{n}} = \boldsymbol{n}\otimes\boldsymbol{n}$ and $\mathrm{I}_{\boldsymbol{\tau}} = \mathrm{I} - \mathrm{I}_{\boldsymbol{n}}$. As mentioned in [2], the low-order ABC (9) acts on spurious reflected P-waves but partially on S-waves. Furthermore, it is not robust in the high-frequency regime (see Section 6). This motivates the investigation of new ABCs. This condition is called LK-ABC in the remaining of the paper.

3. A high-order ABC

Recent works in elastodynamics have proposed accurate approximations of the exact DtN map in the context of the analytical preconditioning technique for boundary integral equations [17,10] and in the context of the On-Surface Radiation conditions method [10]. In this section, we adapt ideas of [10] to construct a high-order ABC for the 2D Navier equation.

3.1. Derivation of an exact DtN operator for the half-plane

Let us consider the case of the half-plane $\Omega^- := \{\boldsymbol{x} = (x, y)^t \in \mathbb{R}^2 : x < 0\}$. The directed normal vector at $\Gamma := \{\boldsymbol{x} \in \mathbb{R}^2 : x = 0\}$ to Ω^- is $\boldsymbol{n} = (1, 0)^t$. The radial direction to Ω^- is x and the tangential one is y. We define the

partial Fourier transform $\hat{\mathbf{f}} := (\hat{f}_1, \hat{f}_2)^t : \mathbb{R}^2 \to \mathbb{R}^2$ of a function $\mathbf{f} := (f_1, f_2)^t : \mathbb{R}^2 \to \mathbb{R}^2$ by

$$\mathcal{F}_{f_j}(x,\xi) = \hat{f}_j(x,\xi) := \int_{\mathbb{R}} f_j(x,y) e^{-iy\xi}\, dy,\ j = 1, 2, \tag{10}$$

and the inverse Fourier by

$$\mathcal{F}^{-1}_{\hat{f}_j}(\boldsymbol{x}) = f_j(\boldsymbol{x}) := \frac{1}{2\pi} \int_{\mathbb{R}} \hat{f}_j(x,\xi) e^{iy\xi}\, d\xi,\ j = 1, 2, \tag{11}$$

with ξ the dual variable of y.

Proposition 1. *For $\Gamma = \{\mathbf{x} = (x, y)^t \in \mathbb{R}^2 : x = 0\}$, the following exact surface relation holds*

$$\boldsymbol{\Lambda}_1 \boldsymbol{u}^+_{|\Gamma} = (\mathrm{I} + \boldsymbol{\Lambda}_2)(\boldsymbol{t}^+_{|\Gamma} - 2\mu \boldsymbol{\mathcal{M}} \boldsymbol{u}^+_{|\Gamma}), \tag{12}$$

with

$$\boldsymbol{\Lambda}_1 = i\rho\omega^2 \left[\boldsymbol{n} (\partial_y^2 + \kappa_p^2 \mathrm{I})^{-1/2} \boldsymbol{n} \cdot \mathrm{I}_{\boldsymbol{n}} + \boldsymbol{\tau} (\partial_y^2 + \kappa_s^2 \mathrm{I})^{-1/2} \boldsymbol{\tau} \cdot \mathrm{I}_{\boldsymbol{\tau}} \right], \tag{13}$$

$$\boldsymbol{\Lambda}_2 = -i \left[\boldsymbol{\tau} (\partial_y (\partial_y^2 + \kappa_s^2 \mathrm{I})^{-1/2} \boldsymbol{n} \cdot \mathrm{I}_{\boldsymbol{n}}) - \boldsymbol{n} (\partial_y (\partial_y^2 + \kappa_p^2 \mathrm{I})^{-1/2} \boldsymbol{\tau} \cdot \mathrm{I}_{\boldsymbol{\tau}}) \right], \tag{14}$$

and $\boldsymbol{\mathcal{M}}$ the Günter tangential derivative which is defined by

$$\boldsymbol{\mathcal{M}} = \partial_y (\boldsymbol{n} \cdot \mathrm{I}_{\boldsymbol{n}}) \boldsymbol{\tau} - \partial_y (\boldsymbol{\tau} \cdot \mathrm{I}_{\boldsymbol{\tau}}) \boldsymbol{n}, \tag{15}$$

where $\boldsymbol{\tau} = (-n_y, n_x)^t := (0, 1)^t$.

Proof. Let us introduce the tangential Günter derivative $\boldsymbol{\mathcal{M}}$ defined by [16, Eq. (1.14) page 282]

$$\boldsymbol{\mathcal{M}} = \frac{\partial}{\partial \boldsymbol{n}} - \boldsymbol{n}\, \mathrm{div} + \boldsymbol{n} \times \mathrm{curl}\,. \tag{16}$$

The traction operator is rewritten

$$\boldsymbol{T} = 2\mu \boldsymbol{\mathcal{M}} + (\lambda + 2\mu)\, \boldsymbol{n}\, \mathrm{div} - \mu \boldsymbol{n} \times \mathrm{curl}\,.$$

We get $\boldsymbol{t}^+_{|\Gamma} - 2\mu \boldsymbol{\mathcal{M}} \boldsymbol{u}^+_{|\Gamma} = ((\lambda + 2\mu)\, \mathrm{div}\, \boldsymbol{u}^+,\ \mu\, \mathrm{curl}\, \boldsymbol{u}^+)^t$. We develop (1) to obtain

$$\begin{cases} (\lambda + 2\mu) \partial_x\, \mathrm{div}\, \boldsymbol{u}^+ - \mu \partial_y\, \mathrm{curl}\, \boldsymbol{u}^+ + \rho\omega^2 u_x^+ = 0, \\ (\lambda + 2\mu) \partial_y\, \mathrm{div}\, \boldsymbol{u}^+ + \mu \partial_x\, \mathrm{curl}\, \boldsymbol{u}^+ + \rho\omega^2 u_y^+ = 0. \end{cases} \tag{17}$$

That leads to

$$\begin{cases} (\lambda + 2\mu) \partial_x\, \mathrm{div}\, \boldsymbol{u}^+ &=& \mu \partial_y\, \mathrm{curl}\, \boldsymbol{u}^+ - \rho\omega^2 u_x^+, \\ \mu \partial_x\, \mathrm{curl}\, \boldsymbol{u}^+ &=& -(\lambda + 2\mu) \partial_y\, \mathrm{div}\, \boldsymbol{u}^+ - \rho\omega^2 u_y^+. \end{cases} \tag{18}$$

We deduce the expression of the first derivative of $\boldsymbol{u}^+$ with respect to x

$$\begin{cases} \partial_x u_x^+ &=& -\dfrac{1}{\rho\omega^2} \left((\lambda + 2\mu) \partial_x^2\, \mathrm{div}\, \boldsymbol{u}^+ - \mu \partial_{xy}\, \mathrm{curl}\, \boldsymbol{u}^+ \right), \\ \partial_x u_y^+ &=& -\dfrac{1}{\rho\omega^2} \left((\lambda + 2\mu) \partial_{xy}\, \mathrm{div}\, \boldsymbol{u}^+ + \mu \partial_x^2\, \mathrm{curl}\, \boldsymbol{u}^+ \right). \end{cases} \tag{19}$$

With the definitions of the Lamé potentials (2), we eliminate the second order derivatives with respect to x as

$$\begin{cases} \partial_x^2\, \mathrm{div}\, \boldsymbol{u}^+ = -\kappa_p^2 \partial_x^2 \psi_p = \kappa_p^2 (\partial_y^2 \psi_p + \kappa_p^2 \psi_p) = -(\partial_y^2 + \kappa_p^2)\, \mathrm{div}\, \boldsymbol{u}^+, \\ \partial_x^2\, \mathrm{curl}\, \boldsymbol{u}^+ = \kappa_s^2 \partial_x^2 \psi_s = -\kappa_s^2 (\partial_y^2 \psi_s + \kappa_s^2 \psi_s) = -(\partial_y^2 + \kappa_s^2)\, \mathrm{curl}\, \boldsymbol{u}^+. \end{cases} \tag{20}$$

We finally obtain

$$\begin{cases} \partial_x u_x^+ &=& \dfrac{1}{\rho\omega^2} \left((\lambda + 2\mu)(\partial_y^2 + \kappa_p^2)\, \mathrm{div}\, \boldsymbol{u}^+ + \mu \partial_{xy}\, \mathrm{curl}\, \boldsymbol{u}^+ \right), \\ \partial_x u_y^+ &=& \dfrac{1}{\rho\omega^2} \left(\mu(\partial_y^2 + \kappa_s^2)\, \mathrm{curl}\, \boldsymbol{u}^+ - (\lambda + 2\mu) \partial_{xy}\, \mathrm{div}\, \boldsymbol{u}^+ \right). \end{cases} \tag{21}$$

• Let us introduce the variable $\mathbf{U} = (\boldsymbol{u}^+, (\lambda + 2\mu)\, \mathrm{div}\, \boldsymbol{u}^+, \mu\, \mathrm{curl}\, \boldsymbol{u}^+)^t$. The Dirichlet trace of $\mathbf{U}$ on Γ is given by $\mathbf{U}_{|\Gamma} = (\boldsymbol{u}^+_{|\Gamma}, \boldsymbol{t}^+_{|\Gamma} - 2\mu \boldsymbol{\mathcal{M}} \boldsymbol{u}^+_{|\Gamma})^t$. We rewrite the elastodynamic system (1) as a first-order hyperbolic system where the

unknown is the Fourier transform of $\mathbf{U}$. Applying the partial Fourier transform along y to systems (21) and (18), we get the equation $A\partial_x\widehat{\mathbf{U}} = B\widehat{\mathbf{U}}$ where

$$A = \begin{pmatrix} I_2 & \frac{1}{\rho\omega^2}M \\ 0_2 & I_2 \end{pmatrix}, \quad \text{with} \quad M = \begin{pmatrix} 0 & -i\xi \\ i\xi & 0 \end{pmatrix}, \tag{22}$$

and

$$B = \begin{pmatrix} 0 & 0 & \frac{\kappa_p^2 - \xi^2}{\rho\omega^2} & 0 \\ 0 & 0 & 0 & \frac{\kappa_s^2 - \xi^2}{\rho\omega^2} \\ -\rho\omega^2 & 0 & 0 & i\xi \\ 0 & -\rho\omega^2 & -i\xi & 0 \end{pmatrix}. \tag{23}$$

• To solve the hyperbolic equation, we introduce the change of variable $\mathbf{V} = A\widehat{\mathbf{U}}$ and write $\partial_x\mathbf{V} = BA^{-1}\mathbf{V}$. The spectrum of BA^{-1} is $\{is_p, is_s, -is_p, -is_s\}$ with $s_p = \sqrt{\kappa_p^2 - \xi^2}$ and $s_s = \sqrt{\kappa_s^2 - \xi^2}$. The matrix is diagonalized as $BA^{-1} = PDP^{-1}$ with $D = diag(-is_p, -is_s, is_p, is_s)$. The associated matrix P is

$$P = \begin{pmatrix} I_2 & I_2 \\ -C & C \end{pmatrix} \quad \text{with} \quad C = i\rho\omega^2 \begin{pmatrix} s_p^{-1} & 0 \\ 0 & s_s^{-1} \end{pmatrix}. \tag{24}$$

The first order hyperbolic system is rewritten as $\partial_x\mathbf{W} = D\mathbf{W}$, for $x \geq 0$, where $\mathbf{W} = P^{-1}\mathbf{V} = P^{-1}A\widehat{\mathbf{U}}$. We get

$$\mathbf{W} = \frac{1}{2}\begin{pmatrix} 1 & 0 & \frac{is_p}{\rho\omega^2} & -\frac{i\xi}{\rho\omega^2} \\ 0 & 1 & \frac{i\xi}{\rho\omega^2} & \frac{is_s}{\rho\omega^2} \\ 1 & 0 & -\frac{is_p}{\rho\omega^2} & -\frac{i\xi}{\rho\omega^2} \\ 0 & 1 & \frac{i\xi}{\rho\omega^2} & -\frac{is_s}{\rho\omega^2} \end{pmatrix}\widehat{\mathbf{U}}. \tag{25}$$

The solution of this equation is $\mathbf{W}(x) = e^{xD}\mathbf{W}(0)$. Since we are characterizing the part of the wave field that is square integrable in the right half-space, then we must impose that the first two components of $\mathbf{W}$ vanish. Coming back to the definition of $\mathbf{U}$, we obtain the equation

$$\widehat{\boldsymbol{u}^+_{|\Gamma}} = \left(-\frac{1}{\rho\omega^2}M + C^{-1}\right)(\widehat{\boldsymbol{t}^+_{|\Gamma}} - 2\mu\boldsymbol{\mathcal{M}}\widehat{\boldsymbol{u}^+_{|\Gamma}}). \tag{26}$$

We multiply by C and we apply the inverse Fourier transform. We have

$$\mathcal{F}^{-1}(C\widehat{\boldsymbol{u}^+_{|\Gamma}}) = i\rho\omega^2\mathcal{F}^{-1}\begin{pmatrix} s_p^{-1}\widehat{u_x} \\ s_s^{-1}\widehat{u_y} \end{pmatrix} = i\rho\omega^2\begin{pmatrix} (\Delta_\Gamma + \kappa_p^2)^{-1/2}u_x \\ (\Delta_\Gamma + \kappa_s^2)^{-1/2}u_y \end{pmatrix} := \boldsymbol{\Lambda}_1\boldsymbol{u}^+_{|\Gamma} \tag{27}$$

and setting $\boldsymbol{q} = \boldsymbol{t}^+_{|\Gamma} - 2\mu\boldsymbol{\mathcal{M}}\boldsymbol{u}_{|\Gamma}$, we get

$$\begin{aligned} \mathcal{F}^{-1}\left(\left(-\frac{1}{\rho\omega^2}CM + I_2\right)\widehat{\boldsymbol{q}}\right) &= \begin{pmatrix} 1 & i\partial_y(\Delta_\Gamma + \kappa_p^2)^{-1/2} \\ -i\partial_y(\Delta_\Gamma + \kappa_s^2)^{-1/2} & 1 \end{pmatrix}\boldsymbol{q} \\ &:= (\mathrm{I} + \boldsymbol{\Lambda}_2)\boldsymbol{q}. \end{aligned} \tag{28}$$

We deduce the surface relation (12). To conclude, we remark that on the boundary Γ of a half-space in the two-dimensional case we have

$$\boldsymbol{\mathcal{M}} = \partial_y(\boldsymbol{n}\cdot\mathrm{I}_{\boldsymbol{n}})\boldsymbol{\tau} - \partial_y(\boldsymbol{\tau}\cdot\mathrm{I}_{\boldsymbol{\tau}})\boldsymbol{n}. \quad \clubsuit$$

3.2. Local approximate DtN operator for a general smooth surface Γ^∞

The surface relation (12) is valid only in the case of an elastic half-plane. There exist two ways to construct such surface operators in the case of a general smooth surface: a formal one using a tangent plane approximation and a rigorous one applying the technique of microlocal diagonalization for hyperbolic systems [3,9,18]. The two approaches allow to obtain

the surface approximation (12), given in of Proposition 1, onto a general smooth surface Γ^∞. At this stage, it gives a non-local ABC, called non-local HO-ABC,

$$\boldsymbol{t}_{|\Gamma^\infty} = \mathcal{B}_1 \boldsymbol{u}_{|\Gamma^\infty} := (\mathrm{I} + \boldsymbol{\Lambda}_2)^{-1} \boldsymbol{\Lambda}_1 \boldsymbol{u}_{|\Gamma^\infty} + 2\mu \boldsymbol{\mathcal{M}} \boldsymbol{u}_{|\Gamma^\infty}, \quad \text{on } \Gamma^\infty, \tag{29}$$

where the operators $\boldsymbol{\Lambda}_1$ and $\boldsymbol{\Lambda}_2$ (see Proposition 1) are expressed by

$$\boldsymbol{\Lambda}_1 = i\rho\omega^2 \left[\boldsymbol{n}(\Delta_\Gamma + \kappa_p^2 \mathrm{I})^{-1/2} \boldsymbol{n} \cdot \mathrm{I}_{\boldsymbol{n}} + \boldsymbol{\tau}(\Delta_\Gamma + \kappa_s^2 \mathrm{I})^{-1/2} \boldsymbol{\tau} \cdot \mathrm{I}_{\boldsymbol{\tau}} \right], \tag{30}$$

$$\boldsymbol{\Lambda}_2 = -i \left[\boldsymbol{\tau}(\partial_s (\Delta_\Gamma + \kappa_s^2 \mathrm{I})^{-1/2} \boldsymbol{n} \cdot \mathrm{I}_{\boldsymbol{n}}) - \boldsymbol{n}(\partial_s (\Delta_\Gamma + \kappa_p^2 \mathrm{I})^{-1/2} \boldsymbol{\tau} \cdot \mathrm{I}_{\boldsymbol{\tau}}) \right], \tag{31}$$

with s the anticlockwise directed curvilinear abscissa along Γ and ∂_s the curvilinear derivative. The Laplace–Beltrami operator over Γ is defined by $\Delta_\Gamma = \partial_s^2$.

The operator $\mathcal{B}_1$ is expressed in terms of inverse of square-root operators. The square-root $z^{1/2}$ of a complex number z stands for the classical complex square-root with branch-cut along the negative real axis. Two ingredients are essential to get an efficient and local ABC. First, a regularization procedure of the square-root operators is needed to improve the accuracy of the approximate DtN $\mathcal{B}_1$ in the zone of grazing modes. The second crucial point is to propose a robust local representation of the square-root operators.

Regularization of the operator $\mathcal{B}_1$.

An artificial singularity of square-root operators occurs in the transition zone from the propagating modes to the evanescent ones. The presence of the singularity does not allow a satisfactory representation of the grazing modes. To model the behavior in the transition zone, we use a regularization by adding a small local damping parameter $\varepsilon_{\{p,s\}} > 0$ to the wavenumber $\kappa_{\{p,s\}}$ [19]. We set $\kappa_{\{p,s\},\varepsilon} := \kappa_{\{p,s\}} + i\varepsilon_{\{p,s\}}$ and we consider square-root operators $\kappa_{\{p,s\}}^{-1} \left(\frac{\Delta_\Gamma}{\kappa_{\{p,s\},\varepsilon}^2} + \mathrm{I} \right)^{-1/2}$ in the ABC (29). We obtain the regularized non-local HO-ABC

$$\boldsymbol{t}_{|\Gamma^\infty} = \mathcal{B}_{1,\varepsilon} \boldsymbol{u}_{|\Gamma^\infty} := (\mathrm{I} + \boldsymbol{\Lambda}_{2,\varepsilon})^{-1} \boldsymbol{\Lambda}_{1,\varepsilon} \boldsymbol{u}_{|\Gamma^\infty} + 2\mu \boldsymbol{\mathcal{M}} \boldsymbol{u}_{|\Gamma^\infty}, \quad \text{on } \Gamma^\infty. \tag{32}$$

Padé-local representation of the operator $\mathcal{B}_{1,\varepsilon}$.

To get a local and uniform representation of the function $(1+z)^{-1/2}$ involved in (30) and (31), we use complex rational Padé approximants with a rotating branch-cut technique of angle α [20]: for $z \in \mathbb{C}$, one has

$$(1+z)^{-1/2} \approx \sum_{\ell=0}^{L-1} \frac{R_\ell^\alpha}{S_\ell^\alpha + z}, \tag{33}$$

where

$$\begin{cases} R_\ell^\alpha = e^{i\alpha/2} c_\ell, \quad S_\ell^\alpha = 1 + e^{i\alpha}(-1 + d_\ell), \quad \ell = 0, \ldots, L-1, \\ c_\ell = \dfrac{d_\ell}{L}, \qquad d_\ell = 1 + \tan^2\left(\dfrac{\pi}{2L} (\dfrac{1}{2} + \ell) \right), \quad \ell = 0, \ldots, L-1. \end{cases} \tag{34}$$

Finally, we propose the following regularized Padé-localized ABC, called HO-ABC in the sequel,

$$\boldsymbol{t}_{|\Gamma^\infty} = \mathcal{B}_{1,\varepsilon}^{\sim} \boldsymbol{u}_{|\Gamma^\infty} := (\mathrm{I} + \boldsymbol{\Lambda}_{2,\varepsilon}^{\sim})^{-1} \boldsymbol{\Lambda}_{1,\varepsilon}^{\sim} \boldsymbol{u}_{|\Gamma^\infty} + 2\mu \boldsymbol{\mathcal{M}} \boldsymbol{u}_{|\Gamma^\infty}, \quad \text{on } \Gamma^\infty, \tag{35}$$

where

$$\begin{aligned} \boldsymbol{\Lambda}_{1,\varepsilon}^{\sim} = {} & i\rho\omega^2 \left[\frac{1}{\kappa_p} \boldsymbol{n} \sum_{\ell=0}^{L-1} R_\ell^\alpha \left(\frac{\Delta_\Gamma}{\kappa_{p,\varepsilon}^2} + S_\ell^\alpha \mathrm{I} \right)^{-1} (\boldsymbol{n} \cdot \mathrm{I}_{\boldsymbol{n}}) \right. \\ & \left. + \frac{1}{\kappa_s} \boldsymbol{\tau} \sum_{\ell=0}^{L-1} R_\ell^\alpha \left(\frac{\Delta_\Gamma}{\kappa_{s,\varepsilon}^2} + S_\ell^\alpha \mathrm{I} \right)^{-1} (\boldsymbol{\tau} \cdot \mathrm{I}_{\boldsymbol{\tau}}) \right], \end{aligned} \tag{36}$$

$$\begin{aligned} \boldsymbol{\Lambda}_{2,\varepsilon}^{\sim} = {} & -i \left[\left(\frac{1}{\kappa_s} \partial_s \sum_{\ell=0}^{L-1} R_\ell^\alpha \left(\frac{\Delta_\Gamma}{\kappa_{s,\varepsilon}^2} + S_\ell^\alpha \mathrm{I} \right)^{-1} (\boldsymbol{n}. \cdot \mathrm{I}_{\boldsymbol{n}}) \right) \boldsymbol{\tau} \right. \\ & \left. - \left(\frac{1}{\kappa_p} \partial_s \sum_{\ell=0}^{L-1} R_\ell^\alpha \left(\frac{\Delta_\Gamma}{\kappa_{p,\varepsilon}^2} + S_\ell^\alpha \mathrm{I} \right)^{-1} (\boldsymbol{\tau} \cdot \mathrm{I}_{\boldsymbol{\tau}}) \right) \boldsymbol{n} \right]. \end{aligned} \tag{37}$$

The choice of damping and Padé parameters will be addressed in the next section.

4. Analytical study in the circular case

In the following, circular scatterer means the cut in the plane (x, y) of a 3D-cylindrical scatterer. In this section, we discuss the accuracy of the LK-ABC (9) and the local HO-ABC (35) in the case of a circular scatterer. This configuration allows to understand analytically the drawbacks and advantages of each ABC and to propose improvements. This study is an interesting preamble to numerical simulations.

4.1. Expression of the analytical solutions

The displacements $\boldsymbol{u}^{+}, \boldsymbol{u}^{0}, \boldsymbol{u}^{1}, \boldsymbol{u}^{1,\varepsilon}$ and $\boldsymbol{u}^{\widetilde{1,\varepsilon}}$, respectively solutions to the exterior problem (1)–(3)–(4) and to the truncated problem (5) associated with the LK-ABC (9), the non-local HO-ABC (29), the non-local HO-ABC after regularization (32) and the HO-ABC (35), are built in this section. The superscript $\star$ will stand for $+$, 0, 1, $(1, \varepsilon)$ or $(\widetilde{1, \varepsilon})$ in the sequel. We describe the general construction of $\boldsymbol{u}^{\star}$ solution to the time-harmonic scattering problem by a rigid elastic disk of radius $r_{\text{int}} > 0$. Following [21,22], we decompose the solution under the form $\boldsymbol{u}^{\star} = \nabla\psi_p^{\star} + \mathbf{curl}\,\psi_s^{\star}$ and since the Lamé potentials $\psi_{\{p,s\}}^{\star}$ are solutions to wave equations (2), the ansatz $\psi_{\{p,s\}}^{\star}(r,\theta) = R_{\{p,s\}}^{\star}(r)\Theta^{\star}(\theta)$ separates equations (2), for $n \in \mathbb{N}$, into

$$\begin{cases} \dfrac{d^2}{d\theta^2}\Theta^{\star} + n^2\Theta^{\star} = 0, \\ \dfrac{d^2}{dr^2}R_{\{p,s\}}^{\star} + \dfrac{1}{r}\dfrac{d}{dr}R_{\{p,s\}}^{\star} + \left(\kappa_{\{p,s\}}^2 - \dfrac{n^2}{r^2}\right)R_{\{p,s\}}^{\star} = 0. \end{cases} \tag{38}$$

The radial part $R_{\{p,s\}}^{\star}$ solves Bessel equations, thus solutions to (38) for $r > r_{\text{int}}$ and $n \in \mathbb{N}$ are given by

$$\begin{cases} \Theta^{\star} = A_n^{\star}\cos(n\theta) + B_n^{\star}\sin(n\theta), \\ R_{\{p,s\}}^{\star} = C_n^{\star}H_n^{(1)}(\kappa_{\{p,s\}}r) + D_n^{\star}H_n^{(2)}(\kappa_{\{p,s\}}r), \end{cases} \tag{39}$$

with $A_n^{\star}$, $B_n^{\star}$, $C_n^{\star}$, $D_n^{\star}$ complex coefficients, $H_n^{(1)}$ and $H_n^{(2)}$ Hankel functions of order n of the first and second kinds respectively. Considering incident plane P-waves of the form $\boldsymbol{u}_p^{\text{inc}}(r,\theta) = \left(\partial_r\phi_p(r,\theta), \frac{\partial_\theta}{r}\phi_p(r,\theta)\right)^t$ with $\phi_p(r,\theta) = e^{-i\kappa_p r\cos(\theta)}$, symmetry with respect to the x-axis requires for all positive integer n: $B_n^{\star} = 0$ in (39) for $\psi_p^{\star}$ and its expansion reads

$$\psi_p^{\star}(r,\theta) = \sum_{n=0}^{\infty}\left[A_{1,n}^{\star}H_n^{(1)}(\kappa_p r) + A_{2,n}^{\star}H_n^{(2)}(\kappa_p r)\right]\cos(n\theta), \tag{40}$$

with $A_{1,n}^{\star}$ and $A_{2,n}^{\star}$ complex coefficients. We deduce in the same way

$$\psi_s^{\star}(r,\theta) = \sum_{n=0}^{\infty}\left[B_{1,n}^{\star}H_n^{(1)}(\kappa_s r) + B_{2,n}^{\star}H_n^{(2)}(\kappa_s r)\right]\sin(n\theta), \tag{41}$$

with $B_{1,n}^{\star}$ and $B_{2,n}^{\star}$ complex coefficients. Due to asymptotic expansions of the Hankel functions for large values of $|z|$ (see [23] 9.2.3 and 9.2.4 p. 364)

$$\begin{cases} H_n^{(1)}(z) & \sim & \sqrt{2/(\pi z)}e^{i(z-1/2n\pi-1/4\pi)}, \\ H_n^{(2)}(z) & \sim & \sqrt{2/(\pi z)}e^{-i(z-1/2n\pi-1/4\pi)}, \end{cases} \tag{42}$$

we remark that the Hankel functions of the first kind are associated to outgoing waves. Coefficients $A_{2,n}^{\star}$ and $B_{2,n}^{\star}$ model the spurious incoming components of the field. In the ideal case when the operator $\mathcal{B}$ is the exact exterior Dirichlet-to-Neumann map, we get $A_{2,n}^{\star} = B_{2,n}^{\star} = 0$ for all modes n. This is the case for the outgoing solution in infinite media and we have $A_{2,n}^{+} = B_{2,n}^{+} = 0$. The efficiency of an ABC is measured by its capability to minimize these coefficients.

Similar expansions can be done in the case of the scattering of incident plane S-waves such that $\boldsymbol{u}_s^{\text{inc}}(r,\theta) = \mathbf{curl}\,\phi_s(r,\theta) = (\frac{1}{r}\partial_\theta\phi_s(r,\theta), -\partial_r\phi_s(r,\theta))^t$ with $\phi_s(r,\theta) = e^{-i\kappa_s r\cos(\theta)}$. To respect the symmetry, the Lamé potentials are given for $r > r_{\text{int}}$ by

$$\begin{cases} \psi_p^{\star,S}(r,\theta) & = & \displaystyle\sum_{n=0}^{\infty}\left[A_{1,n}^{\star,S}H_n^{(1)}(\kappa_p r) + A_{2,n}^{\star,S}H_n^{(2)}(\kappa_p r)\right]\sin(n\theta), \\ \psi_s^{\star,S}(r,\theta) & = & \displaystyle\sum_{n=0}^{\infty}\left[B_{1,n}^{\star,S}H_n^{(1)}(\kappa_s r) + B_{2,n}^{\star,S}H_n^{(2)}(\kappa_s r)\right]\cos(n\theta). \end{cases} \tag{43}$$

We detail in Appendices A–C the calculus of the different spectral coefficients to determine $\boldsymbol{u}^{\star}$ for $\star = +, 0, 1, (1,\varepsilon)$ or $(\widetilde{1,\varepsilon})$ for incident plane P- or S-waves.

Table 1
Diffraction of incident plane P-waves by the unit disk ($\kappa_s = 16\pi$): norm of the errors between the spectral coefficients $A^+_{j,n}$, $j = 1, 2$, of the exact outgoing solution and the spectral coefficients $A^0_{j,n}$ (resp. $A^1_{j,n}$) of the exact solution of the truncated problem with the LK-ABC (resp. the new non-local HO-ABC without damping $(\varepsilon_p, \varepsilon_s) = (0, 0)$) with respect to the parameter δ.

δ	1/4	1	4	8
$\|A^+_1 - A^0_1\|$	1.60	8.26e−01	5.64e−01	3.28e−01
$\|A^+_1 - A^1_1\|$	3.73e−01	1.45e−01	6.48e−02	4.18e−02
$\|B^+_1 - B^0_1\|$	6.38e−01	9.22e−01	3.91e−01	2.89e−01
$\|B^+_1 - B^1_1\|$	4.06e−01	1.60e−01	4.88e−02	2.84e−02
$\|A^+_2 - A^0_2\|$	1.40	8.75e−01	3.8e−01	2.77e−01
$\|A^+_2 - A^1_2\|$	5.40e−01	1.92e−01	5.35e−02	2.74e−02
$\|B^+_2 - B^0_2\|$	1.01	8.76e−01	5.72e−01	3.37e−01
$\|B^+_2 - B^1_2\|$	1.11e−01	1.00e−01	6.09e−02	4.25e−02

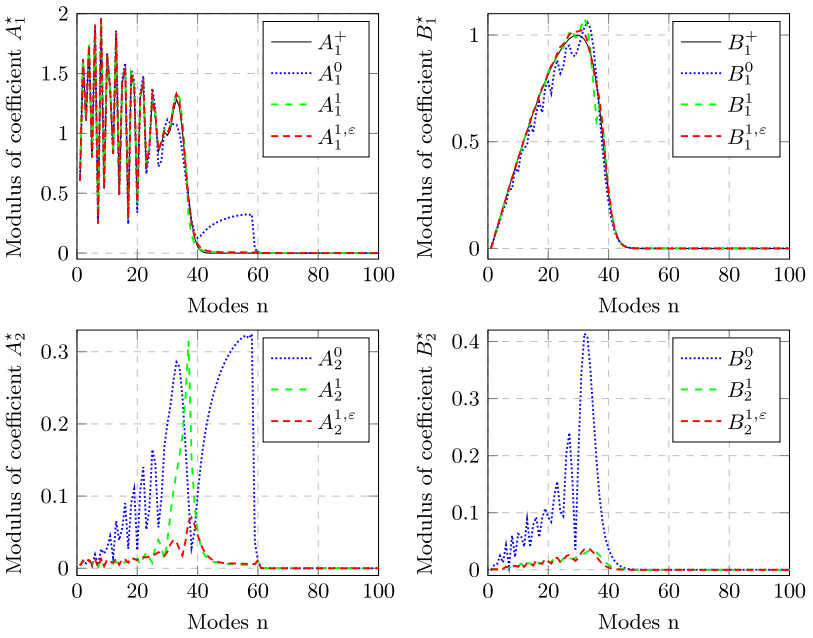

Fig. 3. Diffraction of incident plane P-waves by the unit disk ($\kappa_s = 16\pi$): modulus of the coefficients $A^\star_{1,n}$ (top left), $B^\star_{1,n}$ (top right), $A^\star_{2,n}$ (bottom left), $B^\star_{2,n}$ (bottom right). New non-local HO-ABC without or with regularization process. $\delta = 1/4$, $\varepsilon_{\{p,s\}} = 0$ or $\varepsilon_{\{p,s\}} = 0.39\kappa^{1/3}_{\{p,s\}}(\mathcal{H}^2)^{1/3}$.

4.2. Comparison of the ABCs

4.2.1. Parameter analysis

For the simulations, the physical parameters are $f = 8$ Hz, $\lambda = 0.1$ Pa, $\mu = 1$ Pa and $\rho = 1\,\text{Kg.m}^{-3}$. The wavenumbers satisfy $\kappa_s = 16\pi = \sqrt{2.1}\kappa_p$. We consider incident plane P-waves along x of the form $\boldsymbol{u}^{\text{inc}}_p(\mathbf{x}) = (-i\kappa_p e^{-i\kappa_p x}, 0)^t$. The scatterer is the unit disk. The fictitious boundary $C_{r_{\text{ext}}}$ is at a distance of δ S-wavelengths of the obstacle. Firstly, we study the impact of the distance δ on the errors between the exact outgoing solution and the exact solutions of the truncated problem associated with the LK-ABC (9) and the non-local HO-ABC (29). We report in Table 1 the following norms with respect to δ: $\|A^+_j - A^0_j\|$, $\|B^+_j - B^0_j\|$, $\|A^+_j - A^1_j\|$, $\|B^+_j - B^1_j\|$, $j = 1, 2$, with $A^\star_j = (A^\star_{j,n})_{1\le n\le n_{\max}}$, $B^\star_j = (B^\star_{j,n})_{1\le n\le n_{\max}}$, $\star = +, 0, 1$ (according to the notations of the previous section) and $\|\cdot\|$ the euclidian norm. We fix $n_{\max} = [2\kappa_s]$ where $[\cdot]$ denotes the integer part of a real number.

We recall that the exact outgoing solution satisfies $A^+_2 = B^+_2 = 0$. As expected, errors decrease when the distance δ increases. The contribution of the grazing modes ($n \approx \kappa_p$ and $n \approx \kappa_s$) is more important when the fictitious boundary Γ^∞ is closer to the scatterer. We report in Fig. 3 the modulus of the different spectral coefficients for $\delta = 1/4$. The LK-ABC does not allow to absorb efficiently the propagative and grazing modes.

Table 2
Diffraction of incident plane P-waves by the unit disk ($\kappa_s = 16\pi$): localization errors with respect to the Padé parameters α and L for $\delta = 1/4$ (left) and $\delta = 4$ (right). $\varepsilon_{\{p,s\}} = 0.39\kappa_{\{p,s\}}^{1/3}(\mathcal{H}^2)^{1/3}$.

α	$L=2$	$L=4$	$L=8$	$L=2$	$L=4$	$L=8$
0	9.1e−01	7.1e−01	2.8e−01	1.16e−03	6.8e−07	2.7e-09
$\pi/4$	3.1e−01	4.2e−02	6.6e−03	2.1e−02	4.1e−05	4.5e-10
$\pi/3$	2.7e−01	2.4e−02	4.8e−03	6.4e−02	3.5e−04	1.2e-08
$\pi/2$	4.6e−01	2.7e−02	4.3e−03	3.5e−01	1.0e−02	9.3e-06
$2\pi/3$	1.4	1.5e−01	5.8e−03	1.3	1.4e−01	1.7e-03

Table 3
Diffraction of incident plane P-waves by the unit disk. Comparison between the LK-ABC and the HO-ABC: relative error in euclidian norm on the coefficients of the exact outgoing solution according to the frequency f. $\delta = 8$, $\varepsilon_{\{p,s\}} = 0.39\kappa_{\{p,s\}}^{1/3}(\mathcal{H}^2)^{1/3}$, $L = 4$, $\alpha = \pi/4$.

	$f = 1$ Hz	$f = 2$ Hz	$f = 4$ Hz	$f = 8$ Hz	$f = 16$ Hz
e_r^0	2.4e−02	3.2e−02	4.8e−02	7.2e−02	1.0e-01
$e_r^{(\widetilde{1,\varepsilon})}$	1.3e−02	1.2e−02	1.0e−02	8.9e−03	6.7e-03

The new non-local ABC gives a better accuracy than the low-order one for all coefficients and modes, except for the ingoing P-waves in the transition zone ($n \approx \kappa_p$ and $n \approx \kappa_s$). These localized errors are due to the singularity that arises in the square-root operators. A solution to regularize the square-root operator consists in adding a small artificial damping parameter to the wavenumbers (see Section 3.2). Previous works in acoustics and electromagnetism have exhibited optimal damping parameters by solving optimization problems for a sufficiently large wavenumber in the spherical case [19,24,25]. We consider the same parameters for elastodynamic problems: $\varepsilon_p = 0.39\kappa_p^{1/3}(\mathcal{H}^2)^{1/3}$ and $\varepsilon_s = 0.39\kappa_s^{1/3}(\mathcal{H}^2)^{1/3}$ where $\mathcal{H}$ is the curvature of the boundary Γ^∞. These values of $(\varepsilon_p, \varepsilon_s)$ attenuate efficiently the spurious ingoing P-waves in the transition zone without deteriorating the approximation of the outgoing ones. We observe numerically this improvement in Fig. 3. We consider these two parameters for the regularization in the sequel of the paper. This validates the new non-local HO-ABC even for a small distance between the scatterer and the fictitious boundary. Now, it is important to ensure that the accuracy of the new ABC is preserved after the local representation of the inverse square-root operators. The coefficients, denoted $A_{j,n}^{\widetilde{1,\varepsilon}}, B_{j,n}^{\widetilde{1,\varepsilon}}, j = 1, 2$ (see previous section and Appendix C.1), associated to the HO-ABC (35) depend on the Padé parameters: the angle of rotation α and the order $2L + 1$. We report in Table 2 the localization error

$$e = \sqrt{\|A_1^{1,\varepsilon} - A_1^{\widetilde{1,\varepsilon}}\|^2 + \|B_1^{1,\varepsilon} - B_1^{\widetilde{1,\varepsilon}}\|^2 + \|A_2^{1,\varepsilon} - A_2^{\widetilde{1,\varepsilon}}\|^2 + \|B_2^{1,\varepsilon} - B_2^{\widetilde{1,\varepsilon}}\|^2},$$

according to L and α for $\delta = 1/4$ and $\delta = 4$. The increase of the Padé order leads to better accuracy. An appropriate angle for different distances δ seems to be $\alpha = \pi/4$. When the width of the truncated domain Ω is small, the rotation of the branch-cut plays a major role.

4.2.2. Validation with incident plane P-waves

Finally, we study the robustness of the LK-ABC (9) and the HO-ABC (35) to a frequency increase. We fix $\delta = 8$, $L = 4$ and $\alpha = \pi/4$. We report in Table 3 the relative error in euclidian norm on the coefficients of the exact outgoing solution

$$e_r^\star := \frac{\sqrt{\|A_1^+ - A_1^\star\|^2 + \|B_1^+ - B_1^\star\|^2 + \|A_2^\star\|^2 + \|B_2^\star\|^2}}{\sqrt{\|A_1^+\|^2 + \|B_1^+\|^2}}, \star = 0 \text{ or } (\widetilde{1,\varepsilon}),$$

with respect to the frequency f, setting $n_{\max} = [2\kappa_s]$. The new ABC is more accurate than the low-order one, particularly for high frequencies (error under 0.7% for the new ABC against 10% for the low-order one at $f = 16$ Hz).

4.2.3. Validation with incident plane S-waves

We consider incident plane S-waves along x of the form $\boldsymbol{u}_s^{\text{inc}}(\mathbf{x}) = (0, i\kappa_s e^{-i\kappa_s x})^t$. We use the same physical parameters as in the previous sections. We set the coefficients $\varepsilon_p = 0.39\kappa_p^{1/3}(\mathcal{H}^2)^{1/3}$, $\varepsilon_s = 0.39\kappa_s^{1/3}(\mathcal{H}^2)^{1/3}$, $L = 4$ and $\alpha = \pi/4$ for the Padé approximation. The radius of the obstacle is $r_{\text{int}} = 1$ m and the fictitious boundary is placed at a distance $\delta = 8$ S-wavelengths from the scatterer. We report in Fig. 4 the modulus of the different spectral coefficients for the exact solution to (1)–(3)–(4), the truncated solutions with respectively LK-ABC (9) and the HO-ABC (35). The LK-ABC does not absorb efficiently the propagative and grazing modes and the solution is polluted by non-physical reflections. The HO-ABC gives a better accuracy than the low-order one for all coefficients and modes. The spurious in-going P- and S-waves are efficiently absorbed. The robustness of the new ABC to a frequency increase is confirmed in Table 4.

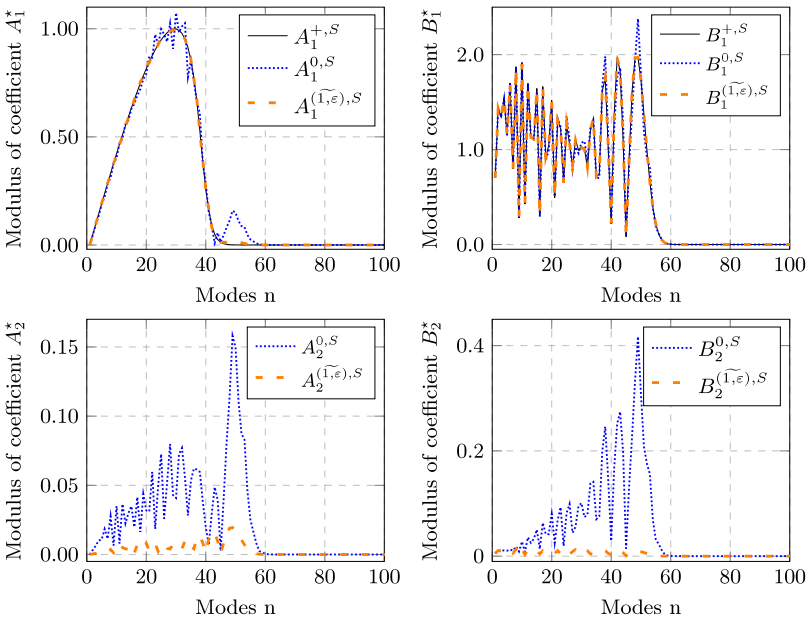

Fig. 4. Diffraction of incident plane S-waves by the unit disk ($\kappa_s = 16\pi$): modulus of the coefficients $A_1^{\star,S}$ (top left), $B_1^{\star,S}$ (top right), $A_2^{\star,S}$ (bottom left), $B_2^{\star,S}$ (bottom right). Comparison between LK-ABC and HO-ABC. $\delta = 8$, $\varepsilon_{\{p,s\}} = 0.39\kappa_{\{p,s\}}^{1/3}(\mathcal{H}^2)^{1/3}$, $L = 4$, $\alpha = \pi/4$.

Table 4
Diffraction of incident plane S-waves by the unit disk. Comparison between the LK-ABC and the HO-ABC: relative error in euclidian norm on the coefficients of the exact outgoing solution according to the frequency f. $\delta = 8$, $\varepsilon_{\{p,s\}} = 0.39\kappa_{\{p,s\}}^{1/3}(\mathcal{H}^2)^{1/3}$, $L = 4$, $\alpha = \pi/4$. $n_{\max} = [2\kappa_s]$.

	$f = 1$ Hz	$f = 2$ Hz	$f = 4$ Hz	$f = 8$ Hz	$f = 16$ Hz
e_r^0	2.9e−02	4.8e−02	8.5e−02	1.5e−01	2.3e-01
$e_r^{(\widetilde{1,\varepsilon})}$	1.7e−02	1.5e−02	1.4e−02	1.2e−02	9.7e-03

5. Finite element implementation

Let us now describe the implementation of the numerical resolution to the truncated Navier problem (5).

Weak formulation. Let us denote $\boldsymbol{u}_g \in (H^1(\Omega))^2$ such that $\boldsymbol{u}_{g_{|\Gamma}} = \boldsymbol{u}^{\text{inc}}$ and $(H_g^1(\Omega))^2 := \left\{\boldsymbol{u} \in (H^1(\Omega))^2 : \boldsymbol{u} = \boldsymbol{u}_g \text{ on } \Gamma\right\}$. Consider a test-function $\boldsymbol{u}' \in (H_0^1(\Omega))^2$, we get the variational formulation: find $\boldsymbol{u} \in (H_g^1(\Omega))^2$ such that

$$\int_\Omega (\sigma(\boldsymbol{u}) : \varepsilon(\boldsymbol{u}') - \rho\omega^2 \boldsymbol{u}\cdot\boldsymbol{u}')d\boldsymbol{x} - \int_{\Gamma^\infty} \mathcal{B}\boldsymbol{u}\cdot\boldsymbol{u}' d\Gamma^\infty = 0, \tag{44}$$

holds for all $\boldsymbol{u}'$. We compare two ABCs on Γ^∞: the Lysmer–Kuhlemeyer boundary condition with $\mathcal{B} = \mathcal{B}_0$ (9) and the HO-ABC which is defined by the operator $\mathcal{B} = \mathcal{B}_{\widetilde{1,\varepsilon}}$ (35). Let us express the term $\int_{\Gamma^\infty} \mathcal{B}\boldsymbol{u}\cdot\boldsymbol{u}' d\Gamma^\infty$ in each case. We use the following notation for the standard scalar product on Γ^∞

$$(\boldsymbol{u}, \boldsymbol{u}') := \int_{\Gamma^\infty} \boldsymbol{u}\cdot\boldsymbol{u}' d\Gamma^\infty. \tag{45}$$

- *LK-ABC*

$$(\mathcal{B}_0\boldsymbol{u}, \boldsymbol{u}') = i(\lambda + 2\mu)\kappa_p(\boldsymbol{n}\cdot\boldsymbol{u}, \boldsymbol{n}\cdot\boldsymbol{u}') + i\mu\kappa_s(\boldsymbol{\tau}\cdot\boldsymbol{u}, \boldsymbol{\tau}\cdot\boldsymbol{u}'). \tag{46}$$

- *HO-ABC*

$$(\mathcal{B}_{\widetilde{1,\varepsilon}}\boldsymbol{u}, \boldsymbol{u}') = ((\mathrm{I} + \boldsymbol{\Lambda}_{\widetilde{2,\varepsilon}})^{-1}\boldsymbol{\Lambda}_{\widetilde{1,\varepsilon}}\boldsymbol{u}, \boldsymbol{u}') + 2\mu(\boldsymbol{\mathcal{M}}\boldsymbol{u}, \boldsymbol{u}'). \tag{47}$$

Recall that the operators $\boldsymbol{\Lambda}_{\widetilde{1,\varepsilon}}$, $\boldsymbol{\Lambda}_{\widetilde{2,\varepsilon}}$ are given by the expressions (36) and (37) respectively. The variational formulation (47) is decomposed into three steps.

Step 1: The coupled variational formulation for the application of the operator $\boldsymbol{\Lambda}_{\widetilde{1,\varepsilon}}$ is given by: find $\boldsymbol{v}$ and the auxiliary scalar variables $v_0, v_1, h_\ell, i_\ell, \ell = 0, \dots, L-1$ such that

$$\begin{cases} (\boldsymbol{v}, \boldsymbol{v}') = i\rho\omega^2(\kappa_p^{-1}(v_0, \boldsymbol{n}\cdot\boldsymbol{v}') + \kappa_s^{-1}(v_1, \boldsymbol{\tau}\cdot\boldsymbol{v}')), \\ (v_0, v_0') = \displaystyle\sum_{\ell=0}^{L-1} R_\ell^\alpha(h_\ell, v_0'), \\ S_\ell^\alpha(h_\ell, h_\ell') - (\kappa_{p,\varepsilon}^{-1}\partial_s h_\ell, \kappa_{p,\varepsilon}^{-1}\partial_s h_\ell') = (\boldsymbol{n}\cdot\boldsymbol{u}, h_\ell'), \quad \ell = 0, \dots, L-1, \\ (v_1, v_1') = \displaystyle\sum_{\ell=0}^{L-1} R_\ell^\alpha(i_\ell, v_1'), \\ S_\ell^\alpha(i_\ell, i_\ell') - (\kappa_{s,\varepsilon}^{-1}\partial_s i_\ell, \kappa_{s,\varepsilon}^{-1}\partial_s i_\ell') = (\boldsymbol{\tau}\cdot\boldsymbol{u}, i_\ell'), \quad \ell = 0, \dots, L-1, \end{cases} \tag{48}$$

holds for all the associated test-functions $\boldsymbol{v}', v_0', v_1', h_\ell', i_\ell', \ell = 0, \dots, L-1$.

Step 2: The coupled variational formulation of the boundary differential equation $(\mathrm{I} + \boldsymbol{\Lambda}_{\widetilde{2,\varepsilon}})\boldsymbol{q} = \boldsymbol{v}$ on Γ^∞, with $\boldsymbol{v} = \boldsymbol{\Lambda}_{\widetilde{1,\varepsilon}}\boldsymbol{u}$ obtained at the Step 1, is expressed by: find $\boldsymbol{q}$ and the auxiliary scalar variables $q_0, q_1, j_\ell, k_\ell, \ell = 0, \dots, L-1$ such that

$$\begin{cases} (\boldsymbol{q}, \boldsymbol{q}') - i\left[\kappa_s^{-1}(\partial_s q_0, \boldsymbol{\tau}\cdot\boldsymbol{q}') - \kappa_p^{-1}\left(\partial_s q_1, \boldsymbol{n}\cdot\boldsymbol{q}'\right)\right] = (\boldsymbol{v}, \boldsymbol{q}'), \\ (q_0, q_0') = \displaystyle\sum_{\ell=0}^{L-1} R_\ell^\alpha(j_\ell, q_0'), \\ S_\ell^\alpha(j_\ell, j_\ell') - (\kappa_{s,\varepsilon}^{-1}\partial_s j_\ell, \kappa_{s,\varepsilon}^{-1}\partial_s j_\ell') = (\boldsymbol{n}\cdot\boldsymbol{q}, j_\ell'), \quad \ell = 0, \dots, L-1, \\ (q_1, q_1') = \displaystyle\sum_{\ell=0}^{L-1} R_\ell^\alpha(k_\ell, q_1'), \\ S_\ell^\alpha(k_\ell, k_\ell') - (\kappa_{p,\varepsilon}^{-1}\partial_s k_\ell, \kappa_{p,\varepsilon}^{-1}\partial_s k_\ell') = (\boldsymbol{\tau}\cdot\boldsymbol{q}, k_\ell'), \quad \ell = 0, \dots, L-1, \end{cases} \tag{49}$$

holds for the associated tests-functions $\boldsymbol{q}', q_0', q_1', j_\ell', k_\ell', \ell = 0, \dots, L-1$.

Step 3: The final step consists in finding an approximation $\boldsymbol{t}$ of the Neumann trace on Γ^∞ such that

$$(\boldsymbol{t}, \boldsymbol{u}') = (\boldsymbol{q}, \boldsymbol{u}') + 2\mu(\boldsymbol{\mathcal{M}}\boldsymbol{u}, \boldsymbol{u}'), \tag{50}$$

where $\boldsymbol{q}$ is computed in Step 2 and $\boldsymbol{\mathcal{M}}$ is the tangential Günter derivative (15).

Finite element discretization. Consider a covering Ω_h of Ω using N_T triangular finite elements with N_V vertices. Let us denote Γ_h and Γ_h^∞ the boundaries of the mesh Ω_h corresponding to Γ and Γ^∞ respectively. Parameter h is the average length of the edges of the triangles. For the discretization, we use classical $\mathbb{P}_1$ finite elements. We denote by $n_{\lambda_s} = \lambda_s/h$ the density of discretization points per S-wavelength. We consider three approximation spaces

$$\begin{cases} \mathbf{U}_h & := & \{\boldsymbol{u}_h \in (\mathcal{C}^0(\Omega))^2 : \boldsymbol{u}_{h|T} \in (\mathbb{P}_1)^2, \forall T \in \Omega_h\} := (\mathbb{P}_1(\Omega_h))^2, \\ \mathbf{U}_{gh} & := & \{\boldsymbol{u}_h \in \mathbf{U}_h : \boldsymbol{u}_h = \boldsymbol{u}_h^{\text{inc}} \text{ on } \Gamma_h\}, \\ \mathbf{V}_h & := & \{\boldsymbol{v}_h \in (\mathcal{C}^0(\Gamma^\infty))^2 : \boldsymbol{v}_{h|T} \in (\mathbb{P}_1)^2, \forall T \in \Gamma_h^\infty\} := (\mathbb{P}_1(\Gamma_h^\infty))^2, \end{cases} \tag{51}$$

with $\dim\mathbf{U}_{gh} = \dim\mathbf{U}_h = 2N_V$ and $\dim\mathbf{V}_h = 2N_b$ where N_b is the number of boundary nodes. Replacing in (46)–(50) $\boldsymbol{u}$ by $\boldsymbol{u}_h \in \mathbf{U}_{gh}$, $(\boldsymbol{v}, \boldsymbol{q}, \boldsymbol{t})$ by $(\boldsymbol{v}_h, \boldsymbol{q}_h, \boldsymbol{t}_h) \in \mathbf{V}_h^3$, (v_0, v_1, q_0, q_1) by $(v_{0,h}, v_{1,h}, q_{0,h}, q_{1,h}) \in \mathbb{P}_1(\Gamma_h^\infty)^4$ and $\forall \ell = 0, \dots, L-1$, $(h_\ell, i_\ell, j_\ell, k_\ell)$ by $(h_{\ell,h}, i_{\ell,h}, j_{\ell,h}, k_{\ell,h}) \in \mathbb{P}_1(\Gamma_h^\infty)^4$, we obtain the discretization of the weak formulation (44) for the LK-ABC and HO-ABC.

The implementation is easy and involves sparse matrices only. The LK-ABC has no additional variables. It requires the resolution of a linear system of size $2N_V$ as the volumic resolution. For the implementation of the HO-ABC, additional variables are needed. In particular, Steps 1 and 2 require each $(2L+4)$ additional variables on Γ_h^∞. It leads to the resolution of a linear system of size $2N_V + 2(2L+4)N_b + 2N_b$. Let us remark that $N_b \ll N_V$.

6. Numerical results

We study the scattering of incident elastic plane waves by the unit disk. The mechanical parameters are chosen such that the wavenumbers satisfy $\kappa_s = \sqrt{2.1}\kappa_p$ ($\lambda = 0.1\,\text{Pa}$, $\mu = 1\,\text{Pa}$, $\rho = 1\,\text{Kg/m}^3$). The fictitious boundary Γ^∞ is the circle of radius $r_{\text{ext}} = 1 + 4\lambda_s$. The truncated computational domain is the annular domain bounded by the unit circle and Γ^∞. The width of the domain is $4\lambda_s$ in order to avoid numerical pollution [26,27], and decreases when the frequency increases (see Table 5). We consider unstructured meshes which are generated using Gmsh software [15]. Fig. 5 reports an example of mesh for $n_{\lambda_s} = 4$ and frequency $f := c_s/\lambda_s = 1$ Hz with c_s the S-wave propagation speed. Physical and mesh parameters are given in Table 5. The simulations are performed with the open source software GetDP [14,28]. All the tests are run on an Intel Core i5-6300U (with two CPU cores 2.40 GHz). The efficiency and accuracy of the HO-ABC depend on different parameters: the damping parameters $\varepsilon_{\{p,s\}}$, the order $2L+1$ and the angle α of the Padé approximation. We summarize the parameters used for all the following simulations (unless indicated otherwise) in Table 6. The choice of the regularizing parameters $\varepsilon_{\{p,s\}}$ and the ones used in the localization process has been discussed in Section 4.

Table 5
Physical parameters and number of degrees of freedom (d.o.f.) corresponding to the simulations ($n_{\lambda_s} = 32$).

f (Hz)	1	2	4	8	16
λ_s (m)	1	1/2	1/4	1/8	1/16
r_{ext} (m)	5	3	2	1.5	1.25
κ_s (rad.m^{-1})	2π	4π	8π	16π	32π
d.o.f. L-K	207 000	274 000	412 000	686 000	1 228 000
d.o.f. Padé	236 000	308 000	457 000	754 000	1 340 000

Table 6
Important parameters of the HO-ABC and corresponding values used in all finite element computations.

Parameters	ε_s	ε_p	L	α
Values	$0.39\kappa_s^{1/3}(\mathcal{H}^2)^{1/3}$	$0.39\kappa_p^{1/3}(\mathcal{H}^2)^{1/3}$	4	$\pi/4$

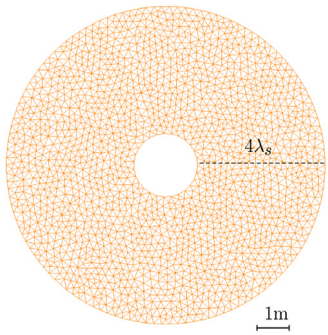

Fig. 5. Example of mesh of the computational domain ($f = 1$ Hz, $n_{\lambda_s} = 4$).

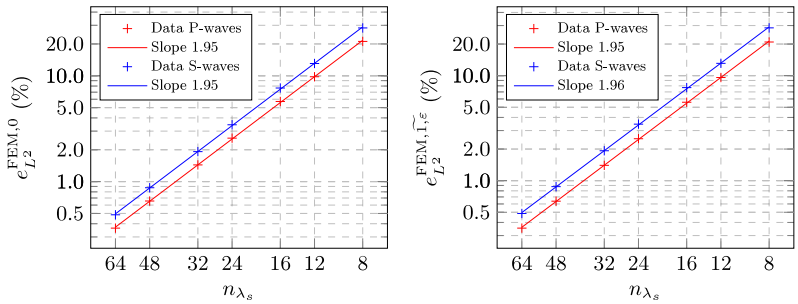

Fig. 6. L2-error $e_{L^2}^{\text{FEM},0}$ (left) and $e_{L^2}^{\text{FEM},\widetilde{1,\varepsilon}}$ (right) in function of refinement of the mesh in logarithm scale. Data and linear regression for incident plane P-waves (red) and S-waves (blue). $f = 1$ Hz. (For interpretation of the references to color in this figure legend, the reader is referred to the web version of this article.)

6.1. Convergence study: validation of the finite element implementation

First, we study the convergence of the finite element method. We consider the scattering of incident plane P-waves $\boldsymbol{u}_p^{\text{inc}}(\mathbf{x}) = (-i\kappa_p e^{-i\kappa_p x}, 0)^t$ or S-waves $\boldsymbol{u}_s^{\text{inc}}(\mathbf{x}) = (0, i\kappa_s e^{-i\kappa_s x})^t$ by the unit disk. We impose on Γ^∞ either the LK-ABC (9) or the HO-ABC (35). We compare truncated analytical solutions $\underset{\sim}{\boldsymbol{u}}^0$ and $\boldsymbol{u}^{(\widetilde{1,\varepsilon})}$ (see Section 4.1, Appendices B and C) with numerical solutions computed with the FEM code (denoted $\boldsymbol{u}_{\text{FEM}}^0$, $\boldsymbol{u}_{\text{FEM}}^{(\widetilde{1,\varepsilon})}$ respectively) thanks to the L2-error

$$e_{L^2}^{\text{FEM},\star} = \frac{\|\boldsymbol{u}_{\text{FEM}}^\star - \boldsymbol{u}^\star\|_{L^2}}{\|\boldsymbol{u}^\star\|_{L^2}}, \quad \star = 0, (\widetilde{1,\varepsilon}). \tag{52}$$

We report in Fig. 6 the L2-error in function of the mesh refinement in logarithm scale. The numerical results corroborate the convergence estimates that predict a theoretical convergence rate of 2 [29]. This validates both the analytic study and the FEM code.

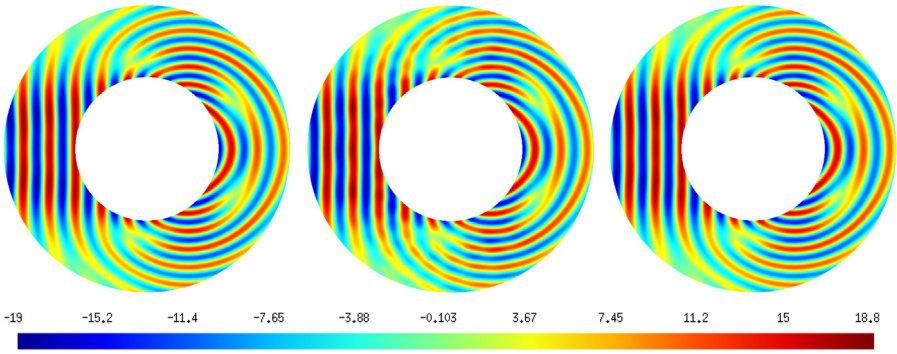

Fig. 7. Real part of the x-component of scattering solution for $f = 4$ Hz (from left to right: analytic solution $\boldsymbol{u}^{+}$, truncated solutions $\boldsymbol{u}^{0}_{\text{FEM}}$ and $\boldsymbol{u}^{(\widetilde{1,\varepsilon})}_{\text{FEM}}$). Displacement in meters for incident plane P-waves. Mesh density $n_{\lambda_s} = 32$. $\delta = 4$, $L = 4$, $\alpha = \pi/4$.

Table 7
Diffraction of incident plane P-waves by the unit disk. Comparison between the LK-ABC and the HO-ABC: L2 error according to the frequency f. $n_{\lambda_s} = 32$, $L = 4$, $\alpha = \pi/4$, $\delta = 4$.

	$f = 1$ Hz	$f = 2$ Hz	$f = 4$ Hz	$f = 8$ Hz	$f = 16$ Hz
$e^{0}_{L_2}$	4.9e−02	6.4e−02	8.9e−02	1.2e−01	1.5e-01
$e^{\widetilde{1,\varepsilon}}_{L_2}$	2.8e−02	2.4e−02	2.2e−02	2.0e−02	1.7e-02

Table 8
Diffraction of incident plane S-waves by the unit disk. Comparison between the LK-ABC and the HO-ABC : L2 error according to the frequency f. $n_{\lambda_s} = 32$, $L = 4$, $\alpha = \pi/4$, $\delta = 4$.

	$f = 1$ Hz	$f = 2$ Hz	$f = 4$ Hz	$f = 8$ Hz	$f = 16$ Hz
$e^{0}_{L_2}$	6.7e−02	9.5e−02	1.5e−01	2.0e−01	2.5e-01
$e^{\widetilde{1,\varepsilon}}_{L_2}$	4.0e−02	3.7e−02	3.2e−02	3.0e−02	2.9e-02

6.2. Numerical efficiency of the high-order ABC

We compare the two ABCs presented in this article: the LK-ABC and the HO-ABC (35) for different frequencies.

6.2.1. Scattering of incident plane P-waves

We consider incident plane P-waves $\boldsymbol{u}^{\text{inc}}_{p}(\mathbf{x}) = (-i\kappa_p e^{-i\kappa_p x}, 0)^t$ striking the unit disk. From now, the L2 error considered is

$$e^{\star}_{L^2} := \frac{\|\boldsymbol{u}^{+} - \boldsymbol{u}^{\star}_{\text{FEM}}\|_{L^2}}{\|\boldsymbol{u}^{+}\|_{L2}}, \quad \star = 0, (\widetilde{1,\varepsilon}). \tag{53}$$

We begin with verifying the robustness of the LK-ABC (9) and HO-ABC (35) to a frequency increase. We report in Table 7 the L2 error of the truncated solutions with respect to the frequency f, setting $n_{\lambda_s} = 32$ points per S-wavelength. As predicted by the analytical study of Section 4.2, the new ABC gives more accurate solutions than the low-order one, especially when increasing the frequency. This is explained by its capability of less generating spurious in-going waves.

Then, we report in Fig. 7 at frequency $f = 4$ Hz the real part of the x-component of the scattered solution in the infinite media $\boldsymbol{u}^{+}$ of the considered problem (1)–(3)–(4) and the truncated solutions $\boldsymbol{u}^{0}_{\text{FEM}}$ with LK-ABC (9) and $\boldsymbol{u}^{(\widetilde{1,\varepsilon})}_{\text{FEM}}$ with HO-ABC (35). We obtain a L2 error of 8.9% with the LK-ABC and of 2.2% applying the HO-ABC. Here, the reflections generated by the fictitious boundary using the LK-ABC are visible in the orthogonal direction of propagation. This drawback is overcome with the high-order ABC. The operator $\mathcal{B}_{\widetilde{1,\varepsilon}}$ (35) is an efficient local approximation of the DtN map.

6.2.2. Scattering of incident plane S-waves

Consider now the scattering of incident plane S-waves $\boldsymbol{u}^{\text{inc}}_{s}(\mathbf{x}) = (0, i\kappa_s e^{-i\kappa_s x})^t$ by the unit disk. We compare in Fig. 8 FE solutions for a frequency $f = 4$ Hz with LK-ABC (9) and HO-ABC (35) to the exact outgoing solution $\boldsymbol{u}^{+,S}$. Here again, we observe multiple spurious reflections with the LK-ABC. They are more pronounced than in the case of incident P-waves. The L2-error is of 15%. The HO-ABC gives a good approximation of the outgoing wave with a L2 error of 3.2%.

We report in Table 8 the L2 error with respect to a frequency increase. This confirms the efficiency of the HO-ABC.

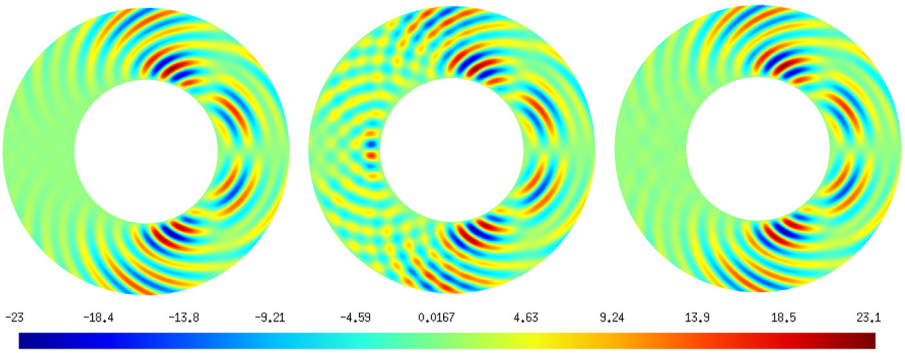

Fig. 8. Real part of the x-component of scattering solution for $f = 4$ Hz (from left to right: analytic solution $\boldsymbol{u}^{+,S}$, truncated solutions $\boldsymbol{u}^{0,S}_{\text{FEM}}$ and $\boldsymbol{u}^{\widetilde{1,\varepsilon},S}_{\text{FEM}}$). Displacement in meters for incident plane S-waves. 32 points per S-wavelength. $\delta = 4, L = 4, \alpha = \pi/4$.

7. Conclusion

In this article, we have proposed a new local ABC, called HO-ABC, for 2D elastic scattering problems. The methodology to construct and to implement this condition is detailed including regularization and localization steps. An analytical study based on an expansion of respectively analytical Navier outgoing solution, solution on truncated domain with low-order LK-ABC or HO-ABC (see Appendices), allows to fix the Padé parameters and compare precisely these two conditions, separating the effects coming from the outgoing and from the ingoing P-waves (wavenumber κ_p) and S-waves (wavenumber κ_s). Numerical results (Section 6) based on a finite element implementation confirm the higher accuracy of the new HO-ABC for frequencies between 1 Hz to 16 Hz. The HO-ABC leads to errors of an order of magnitude lower than classical low-order conditions for an acceptable computational overhead of about 10% in CPU time.

This work constitutes a preamble to future works we want to investigate, especially the use of this new condition as transmission condition in the context of domain decomposition methods without overlap.

Acknowledgment

This research was funded in part through the ARC grant for Concerted Research Actions (ARC WAVES 15/19-03), financed by the Wallonia-Brussels Federation of Belgium.

Appendix A. Analytic Navier outgoing solution

We give the analytical expression of the solution $\boldsymbol{u}^+$ to the exterior problem (1)–(3)–(4) in terms of Hankel functions of the first kind for incident plane P- and S-waves.

A.1. Coefficients for incident plane P-waves

For $r > r_{\text{int}}$, the Lamé potentials associated to the solution $\boldsymbol{u}^+$ to the exterior problem (1)–(3)–(4) are expressed by

$$\begin{cases} \psi_p^+(r,\theta) &= \displaystyle\sum_{n=0}^{\infty} A^+_{1,n} H_n^{(1)}(\kappa_p r)\cos(n\theta), \\ \psi_s^+(r,\theta) &= \displaystyle\sum_{n=0}^{\infty} B^+_{1,n} H_n^{(1)}(\kappa_s r)\sin(n\theta). \end{cases} \tag{A.1}$$

Thus, the cylindrical components $(p^+, q^+)^t := (\partial_r\psi_p^+ + \frac{\partial_\theta}{r}\psi_s^+, \frac{\partial_\theta}{r}\psi_p^+ - \partial_r\psi_s^+)^t$ of the exact displacement field $\boldsymbol{u}^+ := \nabla\psi_p^+ + \mathbf{curl}\,\psi_s^+$ are given by

$$\begin{cases} p^+(r,\theta) &= \displaystyle\sum_{n=0}^{\infty}\Big[A^+_{1,n}\frac{d}{dr}H_n^{(1)}(\kappa_p r) + \frac{n}{r}B^+_{1,n}H_n^{(1)}(\kappa_s r)\Big]\cos(n\theta), \\ q^+(r,\theta) &= \displaystyle\sum_{n=0}^{\infty}\Big[-\frac{n}{r}A^+_{1,n}H_n^{(1)}(\kappa_p r) - B^+_{1,n}\frac{d}{dr}H_n^{(1)}(\kappa_s r)\Big]\sin(n\theta). \end{cases} \tag{A.2}$$

Table A.9
Complex coefficients $m_{ij,n}^{+}$ and $f_{i,n}^{+}$ for $(i,j) \in [\![1,2]\!]^2$.

m_{ij}^{+}	$j=1$	$j=2$	f_i^{+}
$i=1$	$\frac{d}{dr}H_n^{(1)}(\kappa_p r_{\text{int}})$	$\frac{n}{r_{\text{int}}}H_n^{(1)}(\kappa_s r_{\text{int}})$	$-\epsilon_n(-i)^n \frac{d}{dr}J_n(\kappa_p r_{\text{int}})$
$i=2$	$-\frac{n}{r_{\text{int}}}H_n^{(1)}(\kappa_p r_{\text{int}})$	$-\frac{d}{dr}H_n^{(1)}(\kappa_s r_{\text{int}})$	$\epsilon_n(-i)^n \frac{n}{r_{\text{int}}}J_n(\kappa_p r_{\text{int}})$

Table A.10
Complex coefficients $m_{ij,n}^{+,S}$ and $f_{i,n}^{+,S}$ for $(i,j) \in [\![1,2]\!]^2$.

$m_{ij}^{+,S}$	$j=1$	$j=2$	$f_i^{+,S}$
$i=1$	$\frac{d}{dr}H_n^{(1)}(\kappa_p r_{\text{int}})$	$-\frac{n}{r_{\text{int}}}H_n^{(1)}(\kappa_s r_{\text{int}})$	$\epsilon_n(-i)^n \frac{n}{r_{\text{int}}}J_n(\kappa_s r_{\text{int}})$
$i=2$	$\frac{n}{r_{\text{int}}}H_n^{(1)}(\kappa_p r_{\text{int}})$	$-\frac{d}{dr}H_n^{(1)}(\kappa_s r_{\text{int}})$	$\epsilon_n(-i)^n \frac{d}{dr}J_n(\kappa_s r_{\text{int}})$

To build uniquely $\boldsymbol{u}^{+}$, we fix for all positive integer n, $A_{1,n}^{+}$ and $B_{1,n}^{+}$ by substituting the solutions (A.2) into the Dirichlet boundary condition (3) and identifying coefficients of $\cos(n\theta)$ and $\sin(n\theta)$. The incident plane P-waves are expressed by $\boldsymbol{u}_p^{\text{inc}} := (\partial_r \psi_p^{\text{inc}}, \frac{\partial_\theta}{r}\psi_p^{\text{inc}})^t$ with

$$\psi_p^{\text{inc}}(r,\theta) := e^{-i\kappa_p r\cos\theta} = \sum_{n=0}^{\infty} \epsilon_n(-i)^n J_n(\kappa_p r)\cos(n\theta), \tag{A.3}$$

where $\epsilon_0 = 1$ and $\epsilon_n = 2$ for $n \geq 1$ (see [23] 9.1.44 and 9.1.45 p. 361). The Dirichlet boundary condition on $\Gamma := C_{r_{\text{int}}}$ reads $p^{+}(r_{\text{int}},\theta) = -\partial_r \psi_p^{\text{inc}}(r_{\text{int}},\theta)$ and $q^{+}(r_{\text{int}},\theta) = -\frac{\partial_\theta}{r}\psi_p^{\text{inc}}(r_{\text{int}},\theta)$. This results in the linear systems

$$\begin{pmatrix} m_{11,n}^{+} & m_{12,n}^{+} \\ m_{21,n}^{+} & m_{22,n}^{+} \end{pmatrix} \begin{pmatrix} A_{1,n}^{+} \\ B_{1,n}^{+} \end{pmatrix} = \begin{pmatrix} f_{1,n}^{+} \\ f_{2,n}^{+} \end{pmatrix}, \quad \forall n \geq 0, \tag{A.4}$$

with $m_{ij,n}^{+}$ and $f_{i,n}^{+}$ for $(i,j) \in [\![1,2]\!]^2$ given by Table A.9.

A.2. Coefficients for incident plane S-waves

For $r > r_{\text{int}}$, the Lamé potentials associated to the solution to the exterior problem (1)–(3)–(4) are expressed by

$$\begin{cases} \psi_p^{+,S}(r,\theta) &= \displaystyle\sum_{n=0}^{\infty} A_{1,n}^{+,S} H_n^{(1)}(\kappa_p r)\sin(n\theta), \\ \psi_s^{+,S}(r,\theta) &= \displaystyle\sum_{n=0}^{\infty} B_{1,n}^{+,S} H_n^{(1)}(\kappa_s r)\cos(n\theta). \end{cases} \tag{A.5}$$

The cylindrical components $(p^{+,S}, q^{+,S})^t$ of the exact displacement field $\boldsymbol{u}^{+,S}$ are given by

$$\begin{cases} p^{+,S}(r,\theta) &= \displaystyle\sum_{n=0}^{\infty} \left[A_{1,n}^{+} \frac{d}{dr} H_n^{(1)}(\kappa_p r) - \frac{n}{r} B_{1,n}^{+} H_n^{(1)}(\kappa_s r) \right] \sin(n\theta), \\ q^{+,S}(r,\theta) &= \displaystyle\sum_{n=0}^{\infty} \left[\frac{n}{r} A_{1,n}^{+} H_n^{(1)}(\kappa_p r) - B_{1,n}^{+} \frac{d}{dr} H_n^{(1)}(\kappa_s r) \right] \cos(n\theta). \end{cases} \tag{A.6}$$

The considered incident plane S-waves admit the following series expansion

$$\boldsymbol{u}_s^{\text{inc}}(r,\theta) = \sum_{n=0}^{\infty} -\epsilon_n(-i)^n \left(\frac{n}{r} J_n(\kappa_s r)\sin(n\theta), \frac{d}{dr} J_n(\kappa_s r)\cos(n\theta) \right)^t. \tag{A.7}$$

Similarly, we obtain a linear system 2×2 of the form (A.4) (with unknowns the coefficients $A_{1,n}^{+,S}$ and $B_{1,n}^{+,S}$) to solve with $m_{ij,n}^{+,S}$ and $f_{i,n}^{+,S}$ for $(i,j) \in [\![1,2]\!]^2$ given by Table A.10.

Appendix B. Analytic solution on the truncated domain with LK-ABC

The expansions (A.1) and (A.5) are not valid in the case of the truncated problem (5). Non-physical ingoing waves are generated by the fictitious boundary $\Gamma^{\infty} := C_{r_{\text{ext}}}$ and are represented thanks to Hankel functions of the second kind. We fix $r_{\text{ext}} = r_{\text{int}} + \delta\lambda_s$ where $\delta > 0$. In this section, we explicit $\boldsymbol{u}^0$ the analytic scattering Navier outgoing solution in the truncated domain with LK-ABC (9).

Table B.11
Complex coefficients $m^0_{ij,n}$ and $f^0_{i,n}$ for $(i,j) \in [\![1,4]\!]^2$ (with $C_1 = \lambda + 2\mu$, $C_2 = \frac{\lambda}{r_{\text{ext}}} - i\kappa_p(\lambda+2\mu)$, $C_3 = \frac{\mu}{r_{\text{ext}}} + i\kappa_s\mu$). We deduce $m^0_{i2,n}$ and $m^0_{i4,n}$ for $i = [\![1,4]\!]$ substituting $H^{(1)}$ by $H^{(2)}$ in $m^0_{i1,n}$, $m^0_{i3,n}$ respectively.

m^0_{ij}	$j=1$	$j=3$	f^0_i
$i=1$	$m^+_{11,n}$	$m^+_{12,n}$	$f^+_{1,n}$
$i=2$	$m^+_{21,n}$	$m^+_{22,n}$	$f^+_{2,n}$
$i=3$	$C_1\partial_r^2 H_n^{(1)}(\kappa_p r_{\text{ext}})$ $-\frac{\lambda n^2}{r_{\text{ext}}^2} H_n^{(1)}(\kappa_p r_{\text{ext}})$ $+C_2\partial_r H_n^{(1)}(\kappa_p r_{\text{ext}})$	$C_1\partial_r\left(\frac{n}{r_{\text{ext}}} H_n^{(1)}(\kappa_s r_{\text{ext}})\right)$ $-\frac{\lambda n}{r_{\text{ext}}}\partial_r H_n^{(1)}(\kappa_s r_{\text{ext}})$ $+C_2\frac{n}{r_{\text{ext}}} H_n^{(1)}(\kappa_s r_{\text{ext}})$	0
$i=4$	$-\mu\partial_r\left(\frac{n}{r_{\text{ext}}} H_n^{(1)}(\kappa_p r_{\text{ext}})\right)$ $-\mu\frac{n}{r_{\text{ext}}}\partial_r H_n^{(1)}(\kappa_p r_{\text{ext}})$ $+C_3\frac{n}{r_{\text{ext}}} H_n^{(1)}(\kappa_p r_{\text{ext}})$	$-\mu\frac{n^2}{r_{\text{ext}}^2} H_n^{(1)}(\kappa_s r_{\text{ext}})$ $-\mu\partial_r^2 H_n^{(1)}(\kappa_s r_{\text{ext}})$ $+C_3\partial_r H_n^{(1)}(\kappa_s r_{\text{ext}})$	0

B.1. Incident plane P-waves

We denote by $A^0_{j,n}, B^0_{j,n}, j = 1,2$, the coefficients corresponding to the exact solution of the truncated problem with the LK-ABC (9) on Γ^∞ for an incident P-wave. For $r_{\text{int}} \le r \le r_{\text{ext}}$, the Lamé potentials $\psi^0_{\{p,s\}}$ are expressed thanks to (40) and (41). The cylindrical components $(p^0, q^0)^t := (\partial_r\psi^0_p + \frac{\partial_\theta}{r}\psi^0_s, \frac{\partial_\theta}{r}\psi^0_p - \partial_r\psi^0_s)^t$ of the exact displacement field $\boldsymbol{u}^0$ are given by

$$\begin{cases} p^0(r,\theta) &= \displaystyle\sum_{n=0}^{\infty}\Big[A^0_{1,n}\frac{d}{dr}H_n^{(1)}(\kappa_p r) + A^0_{2,n}\frac{d}{dr}H_n^{(2)}(\kappa_p r) \\ &+ \frac{n}{r}B^0_{1,n}H_n^{(1)}(\kappa_s r) + \frac{n}{r}B^0_{2,n}H_n^{(2)}(\kappa_s r)\Big]\cos(n\theta), \\ q^0(r,\theta) &= \displaystyle\sum_{n=0}^{\infty}\Big[-\frac{n}{r}A^0_{1,n}H_n^{(1)}(\kappa_p r) - \frac{n}{r}A^0_{2,n}H_n^{(2)}(\kappa_p r) \\ &- B^0_{1,n}\frac{d}{dr}H_n^{(1)}(\kappa_s r) - B^0_{2,n}\frac{d}{dr}H_n^{(2)}(\kappa_s r)\Big]\sin(n\theta). \end{cases} \tag{B.1}$$

We need four equations for each n to determine the complex coefficients $A^0_{j,n}, B^0_{j,n}, j = 1,2$. The boundary conditions (3) and (9) read

$$\begin{cases} p^0(r_{\text{int}},\theta) &= \displaystyle\sum_{n=0}^{\infty} -\epsilon_n(-i)^n\frac{d}{dr}J_n(\kappa_p r_{\text{int}})\cos(n\theta), \\ q^0(r_{\text{int}},\theta) &= \displaystyle\sum_{n=0}^{\infty}\frac{n}{r_{\text{int}}}\epsilon_n(-i)^n J_n(\kappa_p r_{\text{int}})\sin(n\theta), \\ (\lambda+2\mu)\partial_r p^0(r_{\text{ext}},\theta) &+ \frac{\lambda}{r_{\text{ext}}}\partial_\theta q^0(r_{\text{ext}},\theta) + p^0(r_{\text{ext}},\theta)\left(\frac{\lambda}{r_{\text{ext}}} - i\kappa_p(\lambda+2\mu)\right) = 0, \\ \mu\partial_r q^0(r_{\text{ext}},\theta) &+ \frac{\mu}{r_{\text{ext}}}\partial_\theta p^0(r_{\text{ext}},\theta) - \left(\frac{\mu}{r_{\text{ext}}} + i\kappa_s\mu\right)q^0(r_{\text{ext}},\theta) = 0. \end{cases} \tag{B.2}$$

Replacing p^0, q^0 by (B.1) in (B.2) results in the linear systems

$$\begin{pmatrix} m^0_{11,n} & m^0_{12,n} & m^0_{13,n} & m^0_{14,n} \\ m^0_{21,n} & m^0_{22,n} & m^0_{23,n} & m^0_{24,n} \\ m^0_{31,n} & m^0_{32,n} & m^0_{33,n} & m^0_{34,n} \\ m^0_{41,n} & m^0_{42,n} & m^0_{43,n} & m^0_{44,n} \end{pmatrix}\begin{pmatrix} A^0_{1,n} \\ A^0_{2,n} \\ B^0_{1,n} \\ B^0_{2,n} \end{pmatrix} = \begin{pmatrix} f^0_{1,n} \\ f^0_{2,n} \\ f^0_{3,n} \\ f^0_{4,n} \end{pmatrix}, \quad \forall n \ge 0, \tag{B.3}$$

with $m^0_{ij,n}$ and $f^0_{i,n}$ for $(i,j) \in [\![1,4]\!]^2$ given in Table B.11.

B.2. Incident plane S-waves

We denote by $A^{0,S}_{j,n}, B^{0,S}_{j,n}, j = 1,2$, the coefficients corresponding to the exact solution of the truncated problem with the LK-ABC (9) on Γ^∞ for an incident S-wave $\boldsymbol{u}^{\text{inc}}_s = \mathbf{curl}\,\phi_s = (\frac{\partial_\theta}{r}\phi_s, -\partial_r\phi_s)^t$, with $\phi_s(r,\theta) = e^{-i\kappa_s r\cos(\theta)}$. Similarly, we obtain

Table B.12
Complex coefficients $m_{ij,n}^{0,S}$ and $f_{i,n}^{0,S}$ for $(i,j) \in [\![1,4]\!]^2$. We deduce $m_{i2,n}^{0,S}$ and $m_{i4,n}^{0,S}$ for $i = [\![1,4]\!]$ substituting $H^{(1)}$ by $H^{(2)}$ in $m_{i1,n}^{0,S}$, $m_{i3,n}^{0,S}$ respectively.

$m_{ij,n}^{0,S}$	$j=1$	$j=3$	$f_{i,n}^{0,S}$
$i=1$	$m_{11,n}^{+,S}$	$m_{12,n}^{+,S}$	$f_1^{+,S}$
$i=2$	$m_{21,n}^{+,S}$	$m_{22,n}^{+,S}$	$f_2^{+,S}$
$i=3$	$m_{31,n}^{0}$	$-m_{33,n}^{0}$	0
$i=4$	$-m_{41,n}^{0}$	$m_{43,n}^{0}$	0

a linear system 4×4 to solve. The coefficients of the matrix $m_{ij,n}^{0,S}$ and of the vector $f_{i,n}^{0,S}$ for $(i,j) \in [\![1,4]\!]^2$ are given in Table B.12. Remark that we use coefficients already computed in the infinite media or with incident P-waves.

Appendix C. Analytic solution on the truncated domain with HO-ABC

For $j = 1, 2$, we denote by $A_{j,n}^1, B_{j,n}^1$ the coefficients associated with the new ABC (29); $A_{j,n}^{1,\varepsilon}, B_{j,n}^{1,\varepsilon}$ the coefficients associated with the new ABC after regularization (32) and $A_{j,n}^{\widetilde{1,\varepsilon}}, B_{j,n}^{\widetilde{1,\varepsilon}}$, the coefficients associated with the new ABC after regularization and Padé-localization process (35). We detail in this section the calculus of these different spectral coefficients.

C.1. Incident plane P-waves

For $r_{\text{int}} \leq r \leq r_{\text{ext}}$, the Lamé potentials $\psi_{\{p,s\}}^1$, $\psi_{\{p,s\}}^{1,\varepsilon}$ and $\psi_{\{p,s\}}^{\widetilde{1,\varepsilon}}$ are expressed thanks to (40) and (41). We deduce (see (B.1) in Appendix B) the cylindrical components $(p^1, q^1)^t := (\partial_r \psi_p^1 + \frac{\partial_\theta}{r}\psi_s^1, \frac{\partial_\theta}{r}\psi_p^1 - \partial_r \psi_s^1)^t$, respectively $(p^{1,\varepsilon}, q^{1,\varepsilon})^t$ and $(p^{\widetilde{1,\varepsilon}}, q^{\widetilde{1,\varepsilon}})^t$ of the exact displacement field $\boldsymbol{u}^1$, $\boldsymbol{u}^{1,\varepsilon}$ and $\boldsymbol{u}^{\widetilde{1,\varepsilon}}$ respectively. The boundary condition (29) reads as

$$\mathcal{T}\boldsymbol{u}^1 = \frac{i\rho\omega^2}{1 + \frac{n^2}{r_{\text{ext}}^2}\xi_p\xi_s}\begin{pmatrix}\xi_p p^1 - i\xi_p\xi_s\partial_s q^1 \\ \xi_s q^1 + i\xi_p\xi_s\partial_s p^1\end{pmatrix} + 2\mu\begin{pmatrix}-\partial_s q^1 \\ \partial_s p^1\end{pmatrix},$$

with $\xi_p := (\kappa_p^2 - \frac{n^2}{r_{\text{ext}}^2})^{-1/2}$ and $\xi_s := (\kappa_s^2 - \frac{n^2}{r_{\text{ext}}^2})^{-1/2}$. We explicit (see (B.3) in Appendix B) the coefficients of the matrices $m_{ij,n}^1$ and the vectors $f_{i,n}^1$ for $(i,j) \in [\![1,4]\!]^2$ in Table C.13. To obtain $m_{ij,n}^{1,\varepsilon}$ and $f_{ij,n}^{1,\varepsilon}$ for $(i,j) \in [\![1,4]\!]^2$, we replace ξ_p and ξ_s by

$$\begin{cases}\xi_p^\varepsilon := \dfrac{1}{\kappa_p}\left(1 - \left(\dfrac{n}{\kappa_{p,\varepsilon} r_{\text{ext}}}\right)^2\right)^{-1/2}, \\ \xi_s^\varepsilon := \dfrac{1}{\kappa_s}\left(1 - \left(\dfrac{n}{\kappa_{s,\varepsilon} r_{\text{ext}}}\right)^2\right)^{-1/2}.\end{cases} \tag{C.1}$$

Similarly, to get $m_{ij,n}^{\widetilde{1,\varepsilon}}$ and $f_{ij,n}^{\widetilde{1,\varepsilon}}$ for $(i,j) \in [\![1,4]\!]^2$, we replace ξ_p and ξ_s by

$$\begin{cases}\xi_p^{\widetilde{\varepsilon}} = \dfrac{1}{\kappa_p}\displaystyle\sum_{\ell=0}^{L-1}\frac{R_\ell^\alpha}{S_\ell^\alpha - n^2/(\kappa_{p,\varepsilon} r_{\text{ext}})^2}, \\ \xi_s^{\widetilde{\varepsilon}} = \dfrac{1}{\kappa_s}\displaystyle\sum_{\ell=0}^{L-1}\frac{R_\ell^\alpha}{S_\ell^\alpha - n^2/(\kappa_{s,\varepsilon} r_{\text{ext}})^2}.\end{cases} \tag{C.2}$$

C.2. Incident plane S-waves

We denote by $A_{j,n}^{1,S}, B_{j,n}^{1,S}, j = 1, 2$, respectively $(A_{j,n}^{1,\varepsilon,S}, B_{j,n}^{1,\varepsilon,S})$ and $(A_{j,n}^{\widetilde{1,\varepsilon},S}, B_{j,n}^{\widetilde{1,\varepsilon},S})$, the coefficients associated with the new ABC (29) (respectively the new ABC after regularization (32) and the new ABC (35) after regularization and Padé-localization process) for incident plane S-waves. Similarly, we obtain a linear system 4×4 to solve. The coefficients of the matrix $m_{ij,n}^{1,S}$ and of the vector $f_{i,n}^{1,S}$ for $(i,j) \in [\![1,4]\!]^2$ are given in Table C.14. To obtain $m_{ij,n}^{1,\varepsilon,S}$ and $f_{ij,n}^{1,\varepsilon,S}$ for $(i,j) \in [\![1,4]\!]^2$, we replace in Table C.14 ξ_p and ξ_s by ξ_p^ε, ξ_s^ε defined by (C.1). Similarly, to get $m_{ij,n}^{\widetilde{1,\varepsilon},S}$ and $f_{ij,n}^{\widetilde{1,\varepsilon},S}$, we replace in Table C.14 (ξ_p, ξ_s) by $(\xi_p^{\widetilde{\varepsilon}}, \xi_s^{\widetilde{\varepsilon}})$, see (C.2).

Table C.13
Complex coefficients $m^1_{ij,n}$ and $f^1_{i,n}$ for $(i,j) \in [\![1,4]\!]^2$ (with $D_1 = \lambda + 2\mu$, $D_2 = \frac{\rho\omega^2\xi_p\xi_s}{1+\frac{n^2}{r_{\text{ext}}^2}\xi_p\xi_s}$, $D_3 = \frac{\lambda}{r_{\text{ext}}} - \frac{i\rho\omega^2\xi_p}{1+\frac{n^2}{r_{\text{ext}}^2}\xi_p\xi_s}$, $D_4 = -\frac{\mu}{r_{\text{ext}}} - \frac{i\rho\omega^2\xi_s}{1+\frac{n^2}{r_{\text{ext}}^2}\xi_p\xi_s}$). We deduce $m^1_{i2,n}$ and $m^1_{i4,n}$ for $i = [\![1,4]\!]$ substituting $H^{(1)}$ by $H^{(2)}$ in $m^1_{i1,n}$, $m^1_{i3,n}$ respectively.

$m^1_{ij,n}$	$j=1$	$j=3$	$f^1_{i,n}$
$i=1$	$m^+_{11,n}$	$m^+_{12,n}$	f^+_1
$i=2$	$m^+_{21,n}$	$m^+_{22,n}$	f^+_2
$i=3$	$D_1\partial_r^2 H_n^{(1)}(\kappa_p r_{\text{ext}})$ $+(D_1-D_2)(-n^2/r_{\text{ext}}^2)H_n^{(1)}(\kappa_p r_{\text{ext}})$ $+D_3\partial_r H_n^{(1)}(\kappa_p r_{\text{ext}})$	$D_1\partial_r\left(\frac{n}{r_{\text{ext}}}H_n^{(1)}(\kappa_s r_{\text{ext}})\right)$ $+(D_1-D_2)(-n/r_{\text{ext}})\partial_r H_n^{(1)}(\kappa_s r_{\text{ext}})$ $+D_3(n/r_{\text{ext}})H_n^{(1)}(\kappa_s r_{\text{ext}})$	0
$i=4$	$-\mu\partial_r\left(\frac{n}{r_{\text{ext}}}H_n^{(1)}(\kappa_p r_{\text{ext}})\right)$ $-(D_2-\mu)\frac{n}{r_{\text{ext}}}\partial_r H_n^{(1)}(\kappa_p r_{\text{ext}})$ $-D_4\frac{n}{r_{\text{ext}}}H_n^{(1)}(\kappa_p r_{\text{ext}})$	$-\mu\partial_r^2 H_n^{(1)}(\kappa_s r_{\text{ext}})$ $+(D_2-\mu)\frac{-n^2}{r_{\text{ext}}^2}H_n^{(1)}(\kappa_s r_{\text{ext}})$ $-D_4\partial_r H_n^{(1)}(\kappa_s r_{\text{ext}})$	0

Table C.14
Complex coefficients $m^{1,S}_{ij,n}$ and $f^{1,S}_{i,n}$ for $(i,j) \in [\![1,4]\!]^2$. We deduce $m^{1,S}_{i2,n}$ and $m^{1,S}_{i4,n}$ for $i = [\![1,4]\!]$ substituting $H^{(1)}$ by $H^{(2)}$ in $m^{1,S}_{i1,n}$, $m^{1,S}_{i3,n}$ respectively.

$m^{1,S}_{ij,n}$	1	3	$f^{1,S}_{i,n}$
1	$m^{+,S}_{11,n}$	$m^{+,S}_{12,n}$	$f^{+,S}_1$
2	$m^{+,S}_{21,n}$	$m^{+,S}_{22,n}$	$f^{+,S}_2$
3	$m^1_{31,n}$	$-m^1_{33,n}$	0
4	$-m^1_{41,n}$	$m^1_{43,n}$	0

References

[1] J. Virieux, H. Calandra, R.E. Plessix, A review of the spectral, pseudo-spectral, finite-difference and finite-element modelling techniques for geophysical imaging, Geophys. Prospect. 59 (5) (2011) 794–813.
[2] R. Clayton, B. Engquist, Absorbing boundary conditions for acoustic and elastic wave equation, Bull. Seismol. Soc. Am. 67 (1977) 1529–1540.
[3] B. Engquist, A. Majda, Radiation boundary conditions for acoustic and elastic wave calculations, Comm. Pure Appl. Math. 32 (3) (1979) 314–358.
[4] A. Bayliss, E. Turkel, Radiation boundary condition for wave-like equations, vol. 33 (1980) 707–725.
[5] D. Givoli, J.B. Keller, Non-reflecting boundary conditions for elastic waves, Wave Motion 12 (1990) 261–279.
[6] M.J. Grote, J.B. Keller, Exact nonreflecting boundary condition for elastic waves, SIAM J. Appl. Math. 60 (2000) 803–819.
[7] G.K. Gächter, M.J. Grote, Dirichlet-to-Neumann map for three-dimensional elastic waves, Wave Motion 37 (2003) 293–311.
[8] J. Lysmer, R.L. Kuhlemeyer, Finite dynamic model for infinite media, J. Eng. Mech. Div. ASCE 95 (1969) 859–877.
[9] H. Barucq, M. Bergot, J. Chabassier, E. Estecahandy, Derivation of high order absorbing boundary conditions for the Helmholtz equation in 2D, Research Report RR-8632, INRIA Bordeaux; INRIA, 2014.
[10] S. Chaillat, M. Darbas, F. Le Louër, Approximate local Dirichlet-to-Neumann map for three-dimensional time-harmonic elastic waves, Comput. Methods Appl. Mech. Engrg. 297 (2015) 62–83.
[11] J.P. Berenger, A perfectly matched layer for the absorption of electromagnetic waves, J. Comput. Phys. 114 (2) (1994) 185–200.
[12] W.C. Chew, Q.H. Liu, Perfectly matched layers for elastodynamics: A new absorbing boundary condition, J. Comput. Acoust. 04 (04) (1996) 341–359.
[13] B. Thierry, A. Vion, S. Tournier, M. El Bouaji, D. Colignon, N. Marsic, X. Antoine, C. Geuzaine, GetDDM: An open framework for testing optimized Schwarz methods for time-harmonic wave problems, Comput. Phys. Comm. (203) (2016) 309–330.
[14] P. Dular, C. Geuzaine, F. Henrotte, W. Legros, A general environment for the treatment of discrete problems and its application to the finite element method, IEEE Trans. Magn. 34 (5) (1998) 3395–3398.
[15] C. Geuzaine, J.-F. Remacle, Gmsh: A 3-D finte element mesh generator with built-in pre- and post-processing facilities, Internat. J. Numer. Methods Engrg. 79 (11) (2009) 1309–1331.
[16] V.D. Kupradze, T.G. Gegelia, M.O. Basheleĭshvili, T.V. Burchuladze, Three-dimensional problems of the mathematical theory of elasticity and thermoelasticity, in: V.D. Kupradze (Ed.), Russian ed., in: North-Holland Series in Applied Mathematics and Mechanics, vol. 25, North-Holland Publishing Co., Amsterdam, 1979, p. xix+929.
[17] M. Darbas, F. Le Louër, Well-conditioned boundary integral formulations for the iterative solution of elastic scattering problems, Math. Methods Appl. Sci. 38 (2015) 1705–1733.
[18] X. Antoine, H. Barucq, A. Bendali, Bayliss–turkel-like radiation conditions on surfaces of arbitrary shape, J. Math. Anal. Appl. 229 (1) (1999) 184–211.
[19] X. Antoine, M. Darbas, Y.Y. Lu, An improved surface radiation condition for high-frequency acoustic scattering problems, Comput. Methods Appl. Mech. Engrg. 195 (33–36) (2006) 4060–4074.
[20] S. Chaillat, M. Darbas, F. Le Louër, Fast iterative boundary element methods for high-frequency scattering problems in 3D elastodynamics, J. Comput. Phys. 341 (2017) 429–446.
[21] K. Virta, D. Appelö, Formulae and software for particular solutions to the elastic wave equation in curved geometries, Int. J. Numer. Anal. Methods Geomech. 00 (2016) 1–19.
[22] J.-C. Nédélec, Acoustic and electromagnetic equations, in: Applied Mathematical Sciences, vol. 144, Springer, 2001.
[23] M. Abramowitz, I.A. Stegun, Handbook Of Mathematical Functions with Formulas, Graphs, and Mathematical Tables, 1974.
[24] M. Darbas, Préconditionneurs analytiques de type Calderón pour les formulations intégrales des problèmes de diffraction d'ondes (Ph.D. thesis), INSA, Toulouse, 2004.
[25] M. El Bouajaji, X. Antoine, C. Geuzaine, Approximate local magnetic-to-electric surface operators for time-harmonic Maxwell's equations, J. Comput. Phys. 279 (2014) 241–260.

[26] H. Barucq, A. Bendali, M. Fares, V. Mattesi, S. Tordeux, A symmetric trefftz-dg formulation based on a local boundary element method for the solution of the Helmholtz equation, J. Comput. Phys. 330 (2017) 1069–1092.
[27] F. Ihlenburg, I. Babuška, Finite element solution of the Helmholtz equation with high wave number Part I: The h-version of the FEM, Comput. Math. Appl. 30 (9) (1995) 9–37.
[28] C. Geuzaine, Getdp: A general finite-element solver for the de rham complex, PAMM 7 (2008).
[29] T. Chaumont-Frelet, S. Nicaise, Wavenumber explicit convergence analysis for finite element discretizations of general wave propagation problem, 2018.